

# Broadband Empirical Green's Function Extraction With Data Adaptive Phase Correlations

Sergi Ventosa<sup>1</sup> and Martin Schimmel<sup>1</sup>

**Abstract**—Seismic ambient noise has a strongly nonstationary time-frequency statistics that demand better interstation correlation methods to improve the balance of highly variable ambient-noise sources, reduce the influence of high-energy poorly-distributed signals, and accelerate the convergence to a robust signal or a broadband empirical Green's function (EGF). The wavelet cross-correlation method is convenient to analyze the statistics of the cross-correlation of two signals in terms of lag time and scale/frequency. Here, we introduce wavelet phase cross-correlation (WPCC) functions better adapted to the statistics of seismic ambient noise by combining the ideas of: using only the instantaneous phase information of the phase cross-correlation (PCC) method to assess amplitude unbiasedness, and analyzing cross-correlations scale by scale of the wavelet cross-correlation to balance strong and weak frequency components. These features allow WPCC to extract clean broadband signals useful for seismic imaging and monitoring studies. Further, we analyze and discuss benefits and limitations of WPCC compared to PCC in two examples using low-frequency seismic ambient noise (hum), but results are easily extrapolated to higher frequencies. In hum autocorrelations, WPCC can correct for the baseline and extract cleaner signals, and in hum cross-correlations, can extract richer and more frequency-balanced EGFs allowing for a significant increase of Rayleigh phase- and group-velocity measurements and an improvement of their accuracy. Finally, we offset the increase in computational cost of WPCC compared to PCC by using the graphics processing unit (GPU), and show that WPCC is an efficient approach that permits processing large data volumes as commonly encountered in seismic interferometry studies.

**Index Terms**—Computational seismology, group velocity, interferometry, seismic noise, seismology, surface waves and free oscillations, wavelet transforms.

## I. INTRODUCTION

INTERSTATION correlations are central to interferometry studies at local, regional, and continental scales as, for instance, commonly used to extract surface-wave

Manuscript received 5 September 2022; revised 20 May 2023; accepted 17 June 2023. Date of publication 11 July 2023; date of current version 24 July 2023. This work was supported by the SANIMS Project under Grant RTI2018-095594-B-I00. Sergi Ventosa was also supported in part by the Spanish Ministry of Science and Innovation MCIN/AEI/10.13039/501100011033 and in part by the European Union Next Generation (EU/PRTR) program through the PSI Project under Grant PLEC2021-007875. Martin Schimmel was also supported by the European Union's Horizon Europe research and innovation programme through the AGEMERA project under Grant 10.3030/101058178. ICM has had funding support of the "Severo Ochoa Centre of Excellence" accreditation (CEX2019-000928-S) of the Spanish Research Agency. (*Corresponding author:* Sergi Ventosa.)

Sergi Ventosa was with the Geosciences Barcelona, CSIC, 08028 Barcelona, Spain. He is now with the Institute of Marine Sciences, CSIC, 08003 Barcelona, Spain (e-mail: sventosa@icm.csic.es).

Martin Schimmel is with the Geosciences Barcelona, CSIC, 08028 Barcelona, Spain (e-mail: mschimmel@geo3bcn.csic.es).

Digital Object Identifier 10.1109/TGRS.2023.3294302

empirical Green's functions (EGFs) for seismic tomography. High-quality broadband correlations complement signals from earthquakes in surface-wave tomography and Earth's deep interior studies by sampling otherwise poorly illuminated regions. At regional and continental scales, ambient-noise tomography transformed our ability to image short-wavelength and shallow structures across wide regions, e.g., [1], [2], [3], [4], previously unsatisfactorily resolved due to lack of earthquakes. At global scale, surface-wave tomography is the most powerful method constraining upper-mantle structure and key, together with body-wave and normal-mode observations, to construct high-quality global mantle models, e.g., [5]. The pioneering studies of Nishida et al. [6] and Haned et al. [7] prove the feasibility of ambient-noise tomography for the study of upper-mantle layers with hum sources [8] using stations sparsely distributed around the globe. Short-period observations sampling large regions of the globe, important to constrain the uppermost mantle structure and resolve trade-offs, are still a challenge due to multipathing and attenuation effects arising at the long interstation distances between the seismic stations available. This lack of short periods currently limits our capacity to resolve the short-wavelength velocity structure of the lithosphere-asthenosphere system across large regions of the globe, in particular, underneath the oceanic crust, the Polar regions, and large poorly sampled continental regions such as Africa and Siberia.

Cross-correlation is theoretically sufficient to extract the EGF if ambient-noise sources are well distributed, e.g., [9], [10], [11]. In practice, this is often not satisfied due to the strong nonstationarity of seismic records, and more sophisticated methods are required to improve the balance of sources, reduce the influence of earthquakes and anomalous signals, and increase convergence to EGF or a robust signal extraction of, e.g., the short- and long-period components of surface waves, e.g., [12], [13], [14], [15].

Conventional normalized cross-correlation (NCC) approaches overweight the most energetic signals of the input sequences. The core of the processing flow most often used to reduce the influence of these outlying signals is the 1-bit cross-correlation method [12], [16]. This method applies the cross-correlation on the sign of the input sequences normalized to the number of samples. Since the variance of a zero-mean sequence of 1's and -1's equals to the number of samples, 1-bit NCC (CC1b) measures waveform similarity as sign coherence. Before the correlation operation, the preprocessing often includes spectral whitening to promote a broadband waveform signal at the frequency band of interest [12], [14], or rejects data segments with

anomalous amplitudes [17], [18] to increase convergence. Afterward, the postprocessing may remove correlations with high-coherence values [19] to reduce the contributions from coda waves in ambient-noise correlations, or select and stack only the correlations that constructively contribute to the EGF according to their signal-to-noise ratio [20]. Besides, it may also include denoising operations to increase signal-to-noise ratio such as time-frequency phase-weighted stack (tf-PWS) [21], [22], [23], two-stage time-scale phase-weighted stack (two-stage ts-PWS) [24], and singular value decomposition [25] that filter ambient-noise correlations in transformed domains according to the coherence of their components; or a careful selection and weighting of the main cross-correlation portions according to their root-mean-square value and energy coherency [15].

In exchange for a better balance of noise sources, the 1-bit cross-correlation method introduces waveform distortion and slows down convergence [26]. Phase cross-correlation (PCC) [27] is a less-aggressive alternative to improve waveform coherence and increase convergence [23], [28] that measures waveform similarly as phase coherence, rather than sign coherence, and requires a minimum preprocessing due to its amplitude-unbiased property. These features have been useful, e.g., for monitoring hydromechanical changes [29] or volcanic intrusions [30], imaging geothermal reservoirs [31], extracting reflections from noise autocorrelations at the Moho [32], [33], [34], at shallower subsurface reflections [35], and at the mid-crust and the crust-mantle boundary of Mars [18], constructing a reference Earth model from global earthquake-coda correlations [36], and extracting group-velocity observations from cross-correlations for continental-crust tomography of northwest and west Iberia [37], [38] or global tomography using seismic hum [7] among many other seismic noise interferometry studies.

By measuring waveform similarity as instantaneous phase coherence, PCC reduces the influence of poorly distributed high-energy sources and accelerates convergence without introducing significant waveform distortion. Nevertheless, the main frequency components of the input sequences control the instantaneous phase, e.g., [7] and thus limit the frequency content of surface-wave signals extracted from interstation correlations. Frequency-time normalization (FTN) followed by NCC [13] helps to improve convergence and to extend surface-wave signals to high and low frequencies. Here, instead of using the sign or the phase of frequency or frequency-time normalized sequences to construct a correlation function, we propose to use wavelet cross-correlations [39] as a less-aggressive approach to widen the frequency content of the signals extracted with a minimal preprocessing. Wavelet cross-correlations enable us to define alternative cross-correlation functions better adapted to the highly nonstationary time- and frequency-dependent nature of seismic signals. Basically, the wavelet cross-correlation method decomposes the signals with a set of bandpass filters using the wavelet transform before applying scale-by-scale correlations. This is different than wavelet cospectra and coherence, e.g., [40], [41], [42] that measure instantaneous scale-wise amplitude and phase differences, and coherence

of two data sequences decomposed by the wavelet transform. The wavelet cross-correlation methods, compared to the analogous normalized and phase cross-correlations, can extend frequency content without introducing the waveform distortion of more-aggressive spectral-whitening and data-normalization approaches, provide high-quality broadband signal for ambient-noise and coda correlation studies, and in the context of surface-wave tomography, contribute to resolve short-wavelength and shallow structures in the crust and the uppermost mantle.

## II. WAVELET CROSS-CORRELATIONS

The wavelet cross-correlation method essentially decomposes the input data  $x$  into their scale components and then applies the cross-correlation function at each scale. For the scale decomposition, we use the continuous wavelet transform (CWT) [43], [44]

$$x(\tau, \lambda) = \langle x, \psi_{\tau, \lambda} \rangle = \int_{-\infty}^{\infty} x(t) \frac{1}{\sqrt{\lambda}} \psi^*\left(\frac{t - \tau}{\lambda}\right) dt \quad (1)$$

where  $t$  is time,  $\tau$  is delay or lag time,  $\lambda > 0$  is scale,  $\psi \in L^2(\mathbb{R})$  is a wavelet function,  $\psi^*(t)$  denotes the complex conjugate of  $\psi(t)$ , and  $\langle \cdot, \cdot \rangle$  is the inner product. The wavelet function has zero mean and Euclidean norm equals to one,  $\|\psi\| = 1$ . The  $1/\sqrt{\lambda}$  makes the wavelet family of functions  $\psi_{\tau, \lambda}$  remain normalized  $\|\psi_{\tau, \lambda}\| = 1$ , i.e., average energy remains constant in the transformed domain and therefore the amplitude distribution of white Gaussian noise, e.g., [45]. Then, the wavelet cross-correlation function of the input sequences  $x$  and  $y$  at lag time  $\tau$  and scale  $\lambda$  is given by

$$c_{xy}(\tau, \lambda) = \int_{-\infty}^{\infty} x^*(u, \lambda) y(u + \tau, \lambda) du. \quad (2)$$

Introducing (1) into (2) and rearranging terms, we can recompose the standard cross-correlation function with the following integration along scale:

$$c_{xy}(\tau) = \frac{1}{C_\psi} \int_0^\infty c_{xy}(\tau, \lambda) \frac{d\lambda}{\lambda^2} \quad (3)$$

where

$$C_\psi = \int_0^\infty \frac{|\hat{\psi}(\omega)|^2}{\omega} d\omega \quad (4)$$

is the admissibility condition,  $\omega$  is frequency and  $\hat{\psi}$  is the Fourier transform of  $\psi$  (see Appendix A for a demonstration).

Frames of wavelets are a good approximation of CWT [43] and, in practice, often fast enough to process large data volumes, e.g., [24]. Approximately tight frames (see Appendix B) enable a simple and accurate computation of the wavelet cross-correlation function as

$$c_{xy}[u, s] = \frac{1}{N_s} \sum_{v=0}^{N_s-1} x^*[v, s] y[v + u, s] \quad (5)$$

where  $u$  and  $v$  are the lag-time indexes,  $s$  is the scale index, and  $N_s$  is the number of samples involved in the correlation at each lag time  $u$  and scale  $s$ . Then, the recomposition of the cross-correlation function becomes

$$c_{xy}[u] \simeq \frac{2}{A + B} \sum_{s=0}^{S-1} \frac{1}{a^s} c_{xy}[u, s] \quad (6)$$

in which  $0 < A \leq B < \infty$  are the frame bounds,  $a > 1$  is fixed, and  $a^s$  is the scale, and  $S$  is the number of scales. The  $1/a^s$  term derives from the uniform time-frequency density of a scalogram and the logarithmic sampling along the scale axis.

The functions constructed in (3) and (6) are fully equivalent to the conventional cross-correlation function. The main advantage is the freedom they provide to define cross-correlation functions with a high degree of data adaptability. This approach permits to adapt the cross-correlation to the time-frequency distribution of seismic signals and noise, and therefore achieve a better balance of sources and accelerate convergence to the EGF or a robust signal extraction.

The normalized wavelet cross-correlation improves the balance of signals with different amplitudes distributed across different frequency bands and contributes to extend the frequency content of EGF compared to the standard correlation method, reducing the need of more-aggressive spectral whitening solutions. For instance, the normalized wavelet cross-correlation [39] can be understood as a frequency-wise version of the NCC

$$\begin{aligned} \rho_{xy}[u, s] &= \frac{c_{xy}[u, s]}{\|x_s[v]\| \|y_s[v+u]\|} \\ &= \frac{\sum_v x[v, s] y[v+u, s]}{\sqrt{\sum_v |x[v, s]|^2} \sqrt{\sum_v |y[v+u, s]|^2}} \end{aligned} \quad (7)$$

where  $x_s$  and  $y_s$  are the sequences  $x$  and  $y$  at scale  $s$ , respectively, decomposed using a real or analytic wavelet transform, and often requires regularization to account for a vanishing norm at the denominator. However, this normalization does not help to reduce the influence of earthquakes and anomalous signals. An alternative is to define a frequency-dependent PCC function using an analytic wavelet transform.

The PCC method [27] evaluates similarity of two analytic signals from their unitary phasors. We obtain the phasors by dividing the analytic signal representation of  $x[n]$ ,  $x_a[n] = a[n]e^{i\theta[n]}$ , where  $a$  is the envelope and  $\theta$  is the instantaneous phase, by their modulus,  $e^{i\theta_x[n]} = x_a[n]/|x_a[n]|$  and  $e^{i\theta_y[n]} = y_a[n]/|y_a[n]|$ . The PCC of the input sequences  $x$  and  $y$  is

$$c_{\text{pcc}}[u] = \frac{1}{2N} \sum_{n=0}^{N-1} \left| \frac{e^{i\theta_x[n]} + e^{i\theta_y[n+u]}}{2} \right|^v - \left| \frac{e^{i\theta_x[n]} - e^{i\theta_y[n+u]}}{2} \right|^v \quad (8)$$

where  $N$  is the number of samples correlated and  $v$  is the power of PCC. The PCC ranges from  $-1$  to  $1$  like the NCC, being  $1$  for fully correlated signals,  $0$  for fully uncorrelated and  $-1$  for fully anticorrelated signals.

We obtain the wavelet PCC (WPCC) applying the PCC method along each scale of an analytic wavelet decomposition of the input sequences  $x$  and  $y$ . This is expressed as

$$\begin{aligned} c_{\text{wpcc}}[u, s] &= \frac{1}{2N_s} \sum_{n=0}^{N_s-1} \left| \frac{e^{i\theta_x[n, s]} + e^{i\theta_y[n+u, s]}}{2} \right|^v \\ &\quad - \left| \frac{e^{i\theta_x[n, s]} - e^{i\theta_y[n+u, s]}}{2} \right|^v \end{aligned} \quad (9)$$

that is normalized to an amplitude range of  $-1$  to  $1$ , like its time-domain counterpart. In the particular case of PCC with

$v = 2$  (PCC2), this equation reduces to the real part of the wavelet cross-correlation of the phasors of the analytic wavelet transforms of  $x$  and  $y$  [28]

$$c_{\text{wpcc2}}[u, s] = \text{Re} \left\{ \frac{1}{N_s} \sum_{v=0}^{N_s} \frac{x_a^*[v, s]}{|x_a[v, s]|} \frac{y_a[v+u, s]}{|y_a[v+u, s]|} \right\}. \quad (10)$$

These frequency-dependent PCC functions improve the balances of sources across different frequency bands and, thanks to the amplitude-unbiased property, further reduce the influence of high-energy signals. These features contribute to improve waveform coherence, increase convergence, and extend frequency range of the EGF or a robust signal extraction.

In theory, we can easily obtain good measurements of surface-wave velocity dispersion directly from the above wavelet cross-correlation functions by setting the time-frequency resolution of an analytic wavelet transform according to, e.g., the interstation distance and the signal of interest. Nevertheless, this approach demands a high-redundant frame to sample the continuous wavelet densely enough to obtain accurate observations, with the resulting impact on the computational cost. In the application of the method to field data, as shown further below, a more convenient alternative to allow for frames with much lower redundancies is to construct a cross-correlation function depending only on lag time from the wavelet cross-correlation function, and then apply available methods to measure surface-wave group- and phase-velocity dispersion curves. Following this strategy, we can construct the frequency-dependent PCC2 normalized to a range of  $-1$  to  $1$  as:

$$c_{\text{wpcc2}}[u] = \frac{1-a^S}{1-a} \sum_{s=0}^{S-1} \frac{1}{a^s} c_{\text{wpcc2}}[u, s] \quad (11)$$

where the  $1/a^s$  term in the sum accounts, like in the recombination of the cross-correlation function, for the uniform distribution of the coherence measure of frequency-dependent PCC across the time-frequency domain.

### III. EXAMPLES

In the following examples, we focus on the comparison between the WPCC and PCC methods without spectral-whitening, and spectrally-whitened CC1b and FTN-whitened NCC (FTN-NCC). The performance of PCC compared to conventional and CC1bs from local to global scales has already been shown, e.g., [23], [26], [27].

#### A. Low-Frequency Ambient-Noise Autocorrelations

Without loss of generality, we illustrate the frequency sensitivity of spectrally-whitened CC1b, PCC2, FTN-NCC, and WPCC2 to a mix of high- and low-energy signals using ambient-noise autocorrelations at very long periods of long data sequences from broadband permanent seismic stations. Here, the EGF corresponds to the Green's function for a surface vertical force and thus it is composed mainly of fundamental spheroidal modes. Among them the  ${}_0S_0$  mode is often much stronger than the other fundamental modes

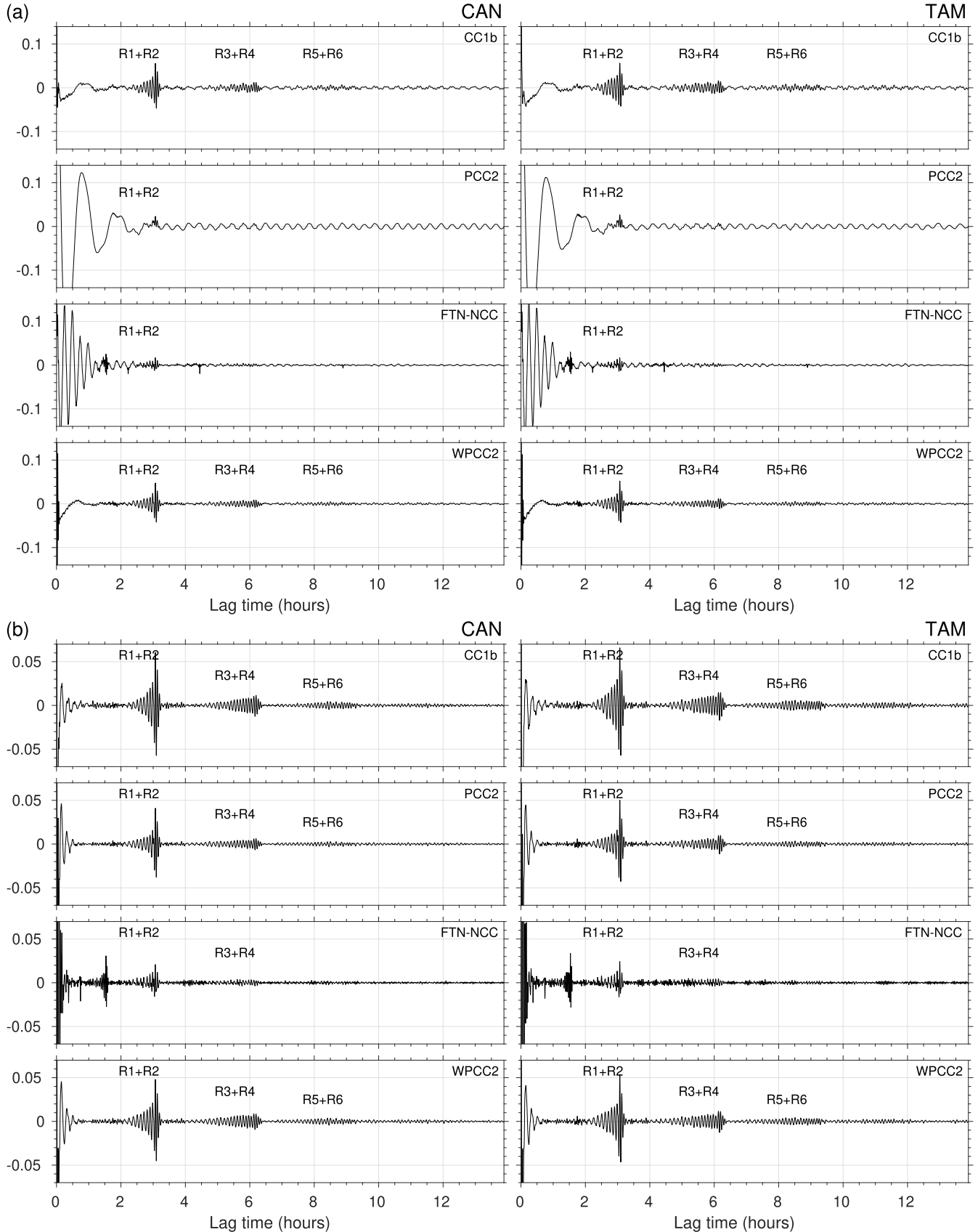


Fig. 1. Portion of ambient-noise autocorrelations of ground acceleration seismograms from the GEOSCOPE stations CAN and TAM at very long periods using spectrally-whitened CC1b, PCC2, FTN-NCC, and WPCC2 at the frequency band of (a) 0.25–10 mHz and (b) 1.5–10 mHz.

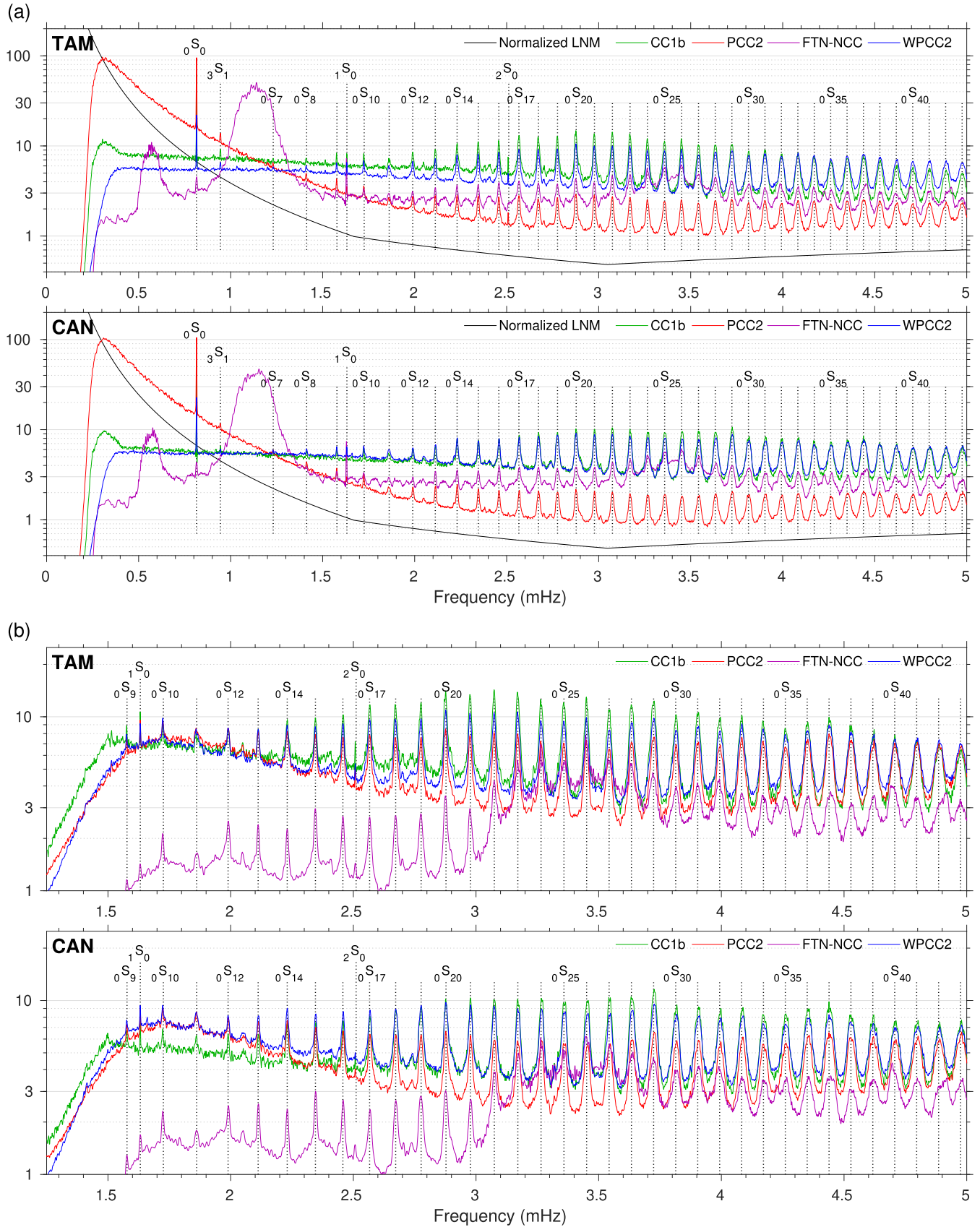


Fig. 2. Amplitude spectra of ambient-noise autocorrelations of ground acceleration seismograms from the GEOSCOPE stations CAN and TAM at very long periods using (green line) spectrally-whitened 1-bit autocorrelation, (red line) PCC2, (purple line) FTN-NCC, and (blue line) WPCC2 at the frequency band of (a) 0.25–10 mHz and (b) 1.5–10 mHz. The black solid line is the LNM of Peterson [47] normalized by the energy in the frequency band of 0.25–10 mHz in (a).

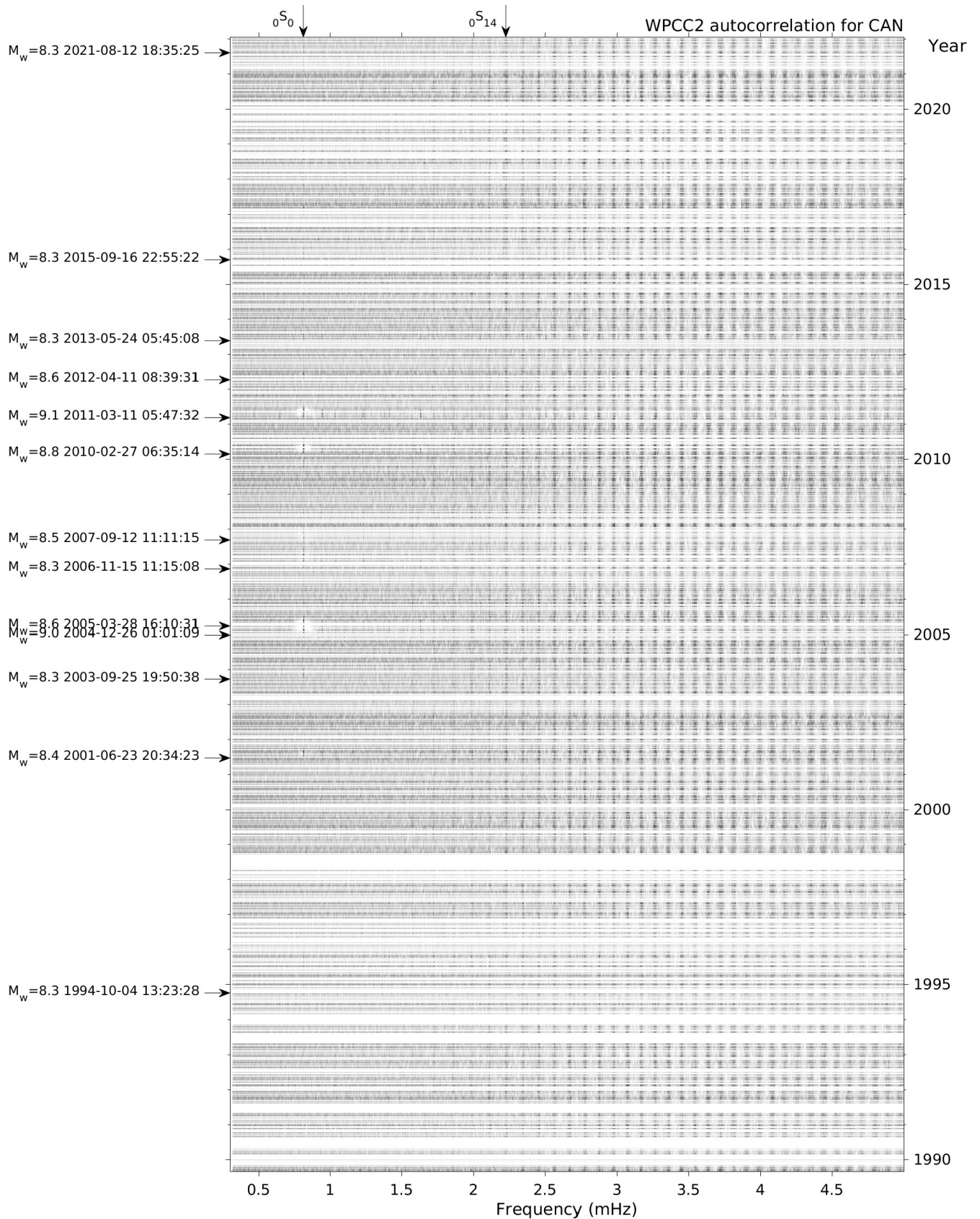


Fig. 3. Spectrogram of ambient-noise WPCC2 autocorrelations of ground acceleration seismograms for the GEOSCOPE station CAN from 1989 to 2021 stacked in Fig. 2. On the left vertical axis, date and centroid time of all earthquakes with a moment magnitude equal or larger than 8.3 in the global CMT catalog. Blank lines correspond to rejected or not available data.

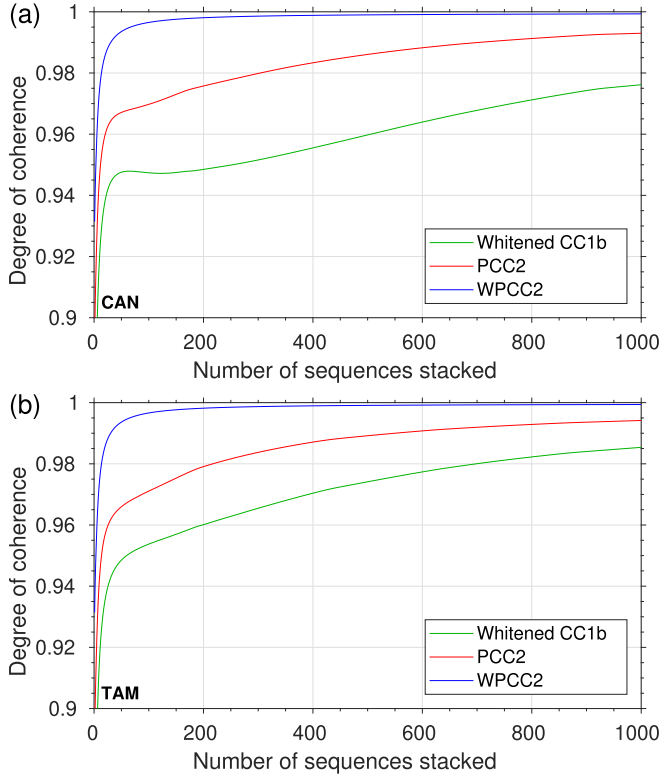


Fig. 4. Convergence to the EGF of stacked noise autocorrelations of the (a) CAN and (b) TAM GEOSCOPE stations shown in Fig. 1(a) extracted using the CC1b method with spectral whitening, and the PCC2 and WPCC2 without.

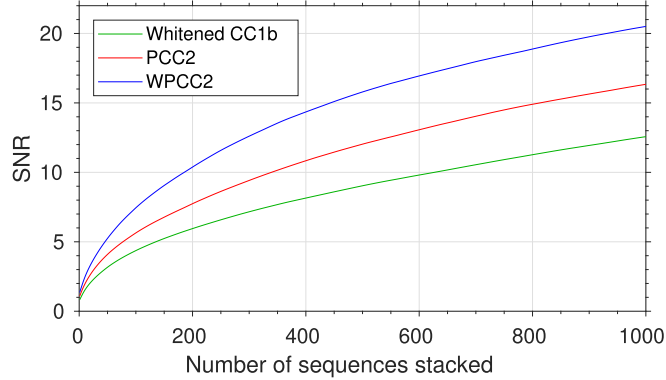


Fig. 5. Variation of the SNR of the  ${}_0S_{14}$  mode with the number of autocorrelations linearly stacked for the GEOSCOPE station CAN, using (green line) spectrally-whitened 1-bit cross-correlation, (red line) PCC2, and (blue line) WPCC2.

observed using ambient-noise correlations [24]. Overtones of spheroidal modes, although much weaker, are eventually observed [46].

We use seismograms for all data available (1989–2021) of the GEOSCOPE stations TAM and CAN. The raw data is corrected to ground acceleration between 0.25 and 10 mHz, filtered with a zero-phase bandpass filter between [see Fig. 1(a)] 0.25 and 10 mHz and [see Fig. 1(b)] 1.5 and 10 mHz, decimated to 0.1 samples/s and cut into five-day-long overlapping segments separated by one day. Besides, we reject sequences containing gaps or high-amplitude signals ( $\text{max} > 100 \text{ MAD}$  where MAD is the median absolute deviation) to

focus on quiet days where ambient-noise sources predominate (see [26]). We computed correlations up to a maximum lag time of  $\pm 400\,000$  s, and stack them linearly after excluding correlations with much higher energy than average due to, e.g., earthquake coda. We whiten the sequences employing the average spectrum of all the data when using the CC1b method because it introduces less noise and signal distortion compared to whitening each sequence individually; and with FTN-NCC, we set the bandwidth of the second-order bandpass Butterworth filters to one-fourth of the lowest frequency as done by default. In the WPCC2 method, we decompose the sequences into their scale components using the Morlet wavelet,  $\psi(t) = \pi^{-1/4} e^{-t^2/2} e^{i\xi_0 t}$  with the default  $\xi_0 = \pi\sqrt{2/\ln 2}$  and six voices per octave from [see Fig. 2(a)] 0.25 and [see Fig. 2(b)] 1.5 mHz, because this wavelet is simple and widespread. Nevertheless, other  $\xi_0$  values on the Morlet wavelet and, in general, any other (pseudo-)analytic wavelet function, such as Mexican Hat, Paul or Morse [48], leading to a convenient time-frequency resolution are appropriate and can potentially improve results. Finally, we compute the spectrum applying a Hann window to the symmetric correlations and then the fast Fourier transform (FFT).

Fig. 1 shows the autocorrelations computed with the CC1b, PCC2, FTN-NCC, and WPCC2 methods, and Fig. 2 the amplitude spectra in logarithmic scale to better see strong and weak signals. We observe the same normal modes using all methods except for the FTN-NCC method where rapid variations on the baseline hinder the observation of fundamental modes below 2 mHz in Fig. 2(a). Besides, the higher amplitude of the  ${}_0S_0$  mode and the lower amplitude of the other modes observed with PCC2 [see Fig. 2(a)] hinders the observation of Rayleigh waves propagating multiple times around the Earth such as  $R3 + R4$  and  $R5 + R6$  with PCC2 [see Fig. 1(a)]. As predicted, the strongest mode observed in Fig. 2(a) is the fundamental spheroidal mode,  ${}_0S_0$ , aside we can see all fundamental modes from about 1 to 5 mHz,  ${}_0S_l$  with  $l \geq 7$ , and a few higher modes ( ${}_1S_0$ ,  ${}_2S_0$  and  ${}_3S_1$ ) far from the resonance frequencies of the fundamental modes. The relative amplitudes of the higher modes are similar with all methods except with FTN-NCC where  ${}_1S_0$  is stronger while  ${}_2S_0$  and  ${}_3S_1$  are not detected. Rejecting sequences with high amplitude signals and anomalous correlations greatly reduces the contribution of earthquake coda and the amplitude of body-wave signal extracted from ambient-noise correlations. However, we do not expect to fully remove the contribution of coda considering that normal modes excited with very strong earthquakes are detected after a few weeks due to their low attenuation, particularly  ${}_0S_0$  and the higher modes we observe due to their very low attenuation values ( $Q > 1000$ ). This is verified in Fig. 3 where we show the amplitude spectra of the WPCC2 autocorrelations sorted into chronological order and linearly stacked with a moving window of 33 sequences. We observe the fundamental modes with  $l \geq 7$  across all correlations clearly; in contrast to  ${}_0S_0$  and the higher modes we observe that arise after main earthquakes and almost disappears in the most quiet time periods. This is reasonable considering that ambient-noise sources locate on the Earth's surface.

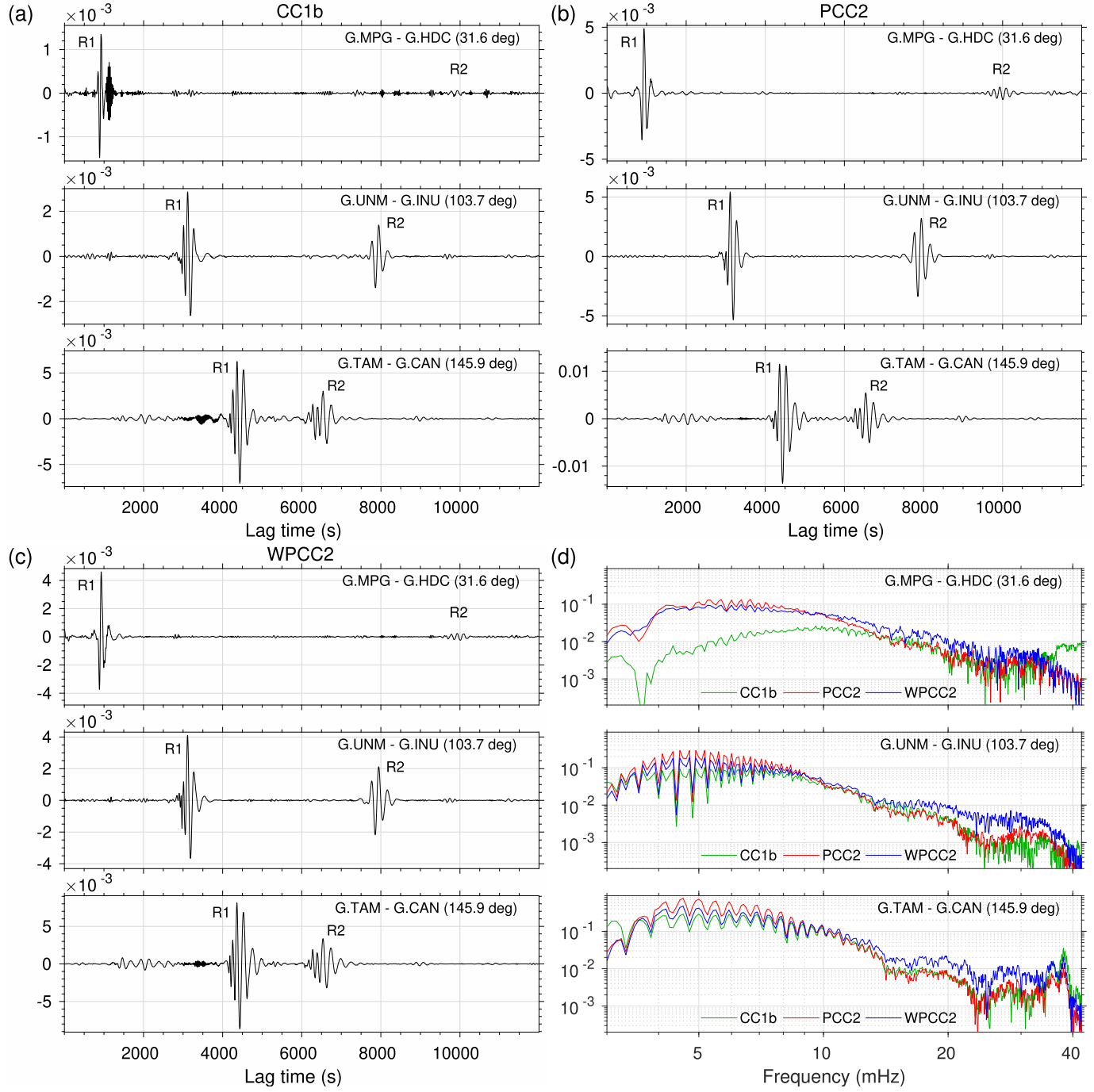


Fig. 6. Ambient-noise cross-correlations of ground-velocity data bandpass filtered from 4 to 32 mHz using (a) spectrally-whitened CC1b, (b) PCC2, and (c) WPCC2 at three interstation distances, and (d) their amplitude spectra.

A key feature in observing the spectral variations of EGF over time shown in Fig. 3 is to achieve fast convergence, or more precisely, to reach high signal-to-noise levels, particularly in individual normal modes, using the minimum data. Fig. 4 shows convergence as the average degree of coherence between the autocorrelations displayed in Fig. 1(a) and all possible linear stacks of  $n$  consecutive autocorrelations, and similarly, Fig. 5 shows the average variation of the signal-to-noise amplitude ratio (SNR) of the  ${}_0S_{14}$  mode. Where we measure SNR as the ratio of the amplitude of the mode from the baseline relative to the standard variation of the

noise in between neighboring fundamental normal modes. We observe in Fig. 4 that the WPCC2 method has a much faster convergence than the PCC2 and CC1b methods. More precisely, WPCC2 reaches roughly the same SNR of PCC with 60% of the data and of spectrally-whitened CC1b with 30% of the data in the  ${}_0S_{14}$  mode (see Fig. 5).

A main difference between these methods resides in the baseline. The baseline of the PCC2 autocorrelation is approximately the spectrum of the output noise of the seismometer divided by its variance and, as can be seen in [26, Fig. 3], follows the same trend as the NCC. As a result, the power

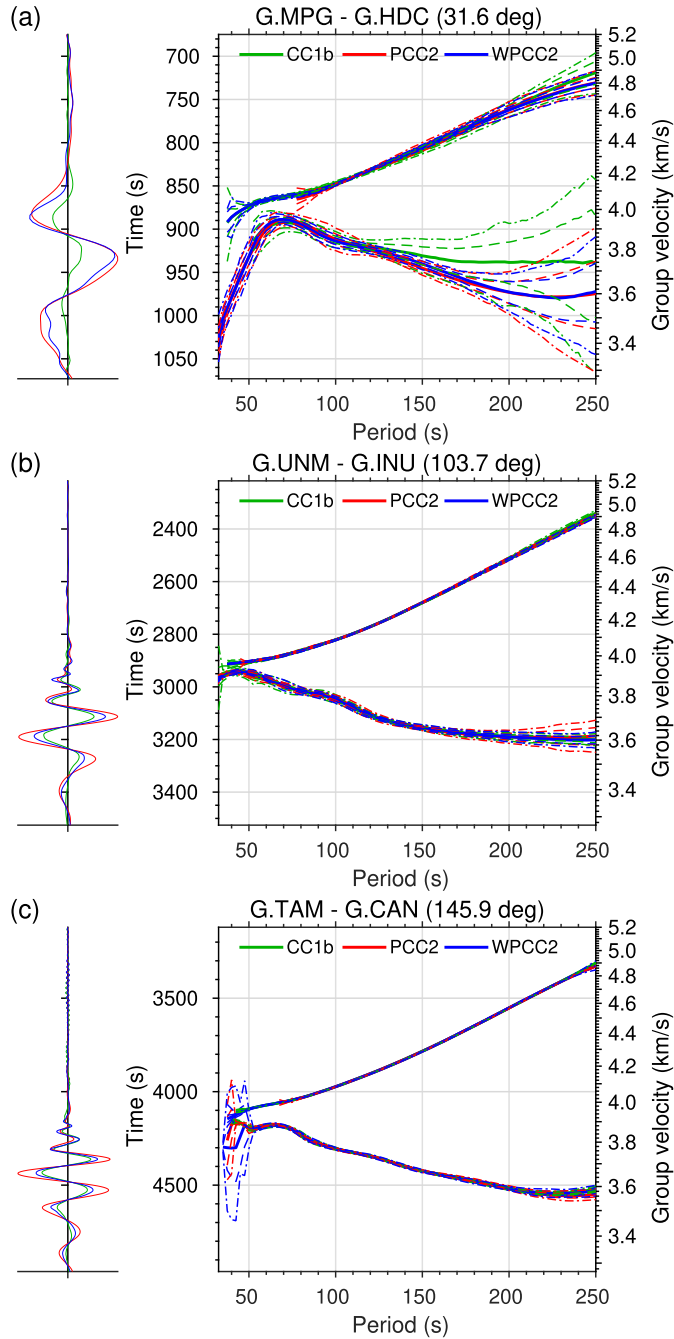


Fig. 7. Velocity dispersion curves extracted from the minor-arc Rayleigh waves ( $R1$ ) from (a) MPG-HDC, (b) UNM-INU, and (c) TAM-CAN GEOSCOPE station pairs shown in Fig. 6(a) and (b), enlarged on the left-hand side, using jackknife resampling. Solid lines are average phase and group velocity, dash-dotted lines the 95% confidence interval, and dashed lines the confidence interval for standard deviation.

noise level for the vertical channel of the CAN and TAM GEOSCOPE stations determines the baseline of PCC2 spectra shown in Fig. 2(a). These stations use STS-1 broadband seismometers and have a noise level close to the low noise model (LNM) of Peterson [47] at frequencies below 50 mHz [49]. Hence, the baseline of the PCC2 spectra is close to LNM normalized by the variance of the noise in the 0.25–10 mHz frequency band. In contrast, the baseline of the WPCC2 and spectrally-whitened 1-bit autocorrelations are approximately flat in the frequency range analyzed because the noise

spectrum of the seismometer is roughly normalized only by the variance of the noise at each scale (i.e., frequency band) in WPCC2 or by the amplitude spectrum of the noise in CC1b. The WPCC2 and CC1b amplitude spectra (see Fig. 2) are similar, the relative amplitude of the normal modes is higher for CC1b and the spectrum is smoother for WPCC2. In addition, the relative amplitude of the normal modes with WPCC2 is slightly higher than with PCC2 because the SNR at each scale increases and the envelope normalization done to compute the unitary phasors is adapted to each frequency band. When we reduce the frequency band analyzed to the frequency range where the variations of the seismic background-noise level are smaller, Fig. 2(b), the PCC2 level increases and becomes much closer to the spectra of WPCC2.

### B. Phase- and Group-Velocity Measurement of Seismic Hum

A key application of ambient-noise correlations is providing the data set of surface-wave signals required to construct tomographic models, conventionally from observations of group- and phase-velocity dispersion, e.g., [3], [4], [37], [50], although full-waveform approaches are also possible, e.g., [51]. In this example, we compare the number and accuracy of Rayleigh-wave group-velocity dispersion curves extracted from interstation correlations of sequences from broadband seismic stations in the hum (4–32 mHz) frequency band using CC1b, PCC2 and WPCC2.

Surface waves extracted from ambient-noise interstation correlations can sample wide regions of the globe with a better coverage inherent to a better distribution of station pairs in comparison to earthquake-station pairs. This is because strong earthquakes occur mostly at plate boundaries, limiting therefore wave path distribution. Nishida et al. [6] demonstrate with limited Rayleigh phase-velocity data that the seismic hum can be used to construct a global upper-mantle model of S-wave velocity. Following this work, Haned et al. [7] increase lateral resolution and resolve shallower structure with a much larger and accurate Rayleigh group-velocity dataset. More recently, Sager et al. [51] prove that full-waveform ambient-noise tomography can be used to resolve upper-mantle structure and noise source distribution jointly without the need of extracting the EGF. To attain the resolution and capacity of resolving structure of global upper-mantle models constructed from earthquake sources, we have to increase the number of surface-wave observations and improve their quality, particularly, at short periods.

In this test, we use all data available (until 2019) of a selection of 376 high-quality broadband seismic stations well distributed around the globe from main global and regional seismic networks of the Alaska regional network (AK), national tsunami warning center Alaska seismic network (AT), Geoscience Australia (AU), GEOSCOPE (G), GEOFON (GE), new China Digital Network (IC), GSN (II, IU), Chilean National Seismic Network (C), Canadian National Seismograph Network (CN), Caribbean USGS network (CU), Danish Seismological Network (DK), Northern Finland Seismological Network (FN), Global Telemetered Seismograph Network (GT), Mediterranean Very Broadband Seismographic

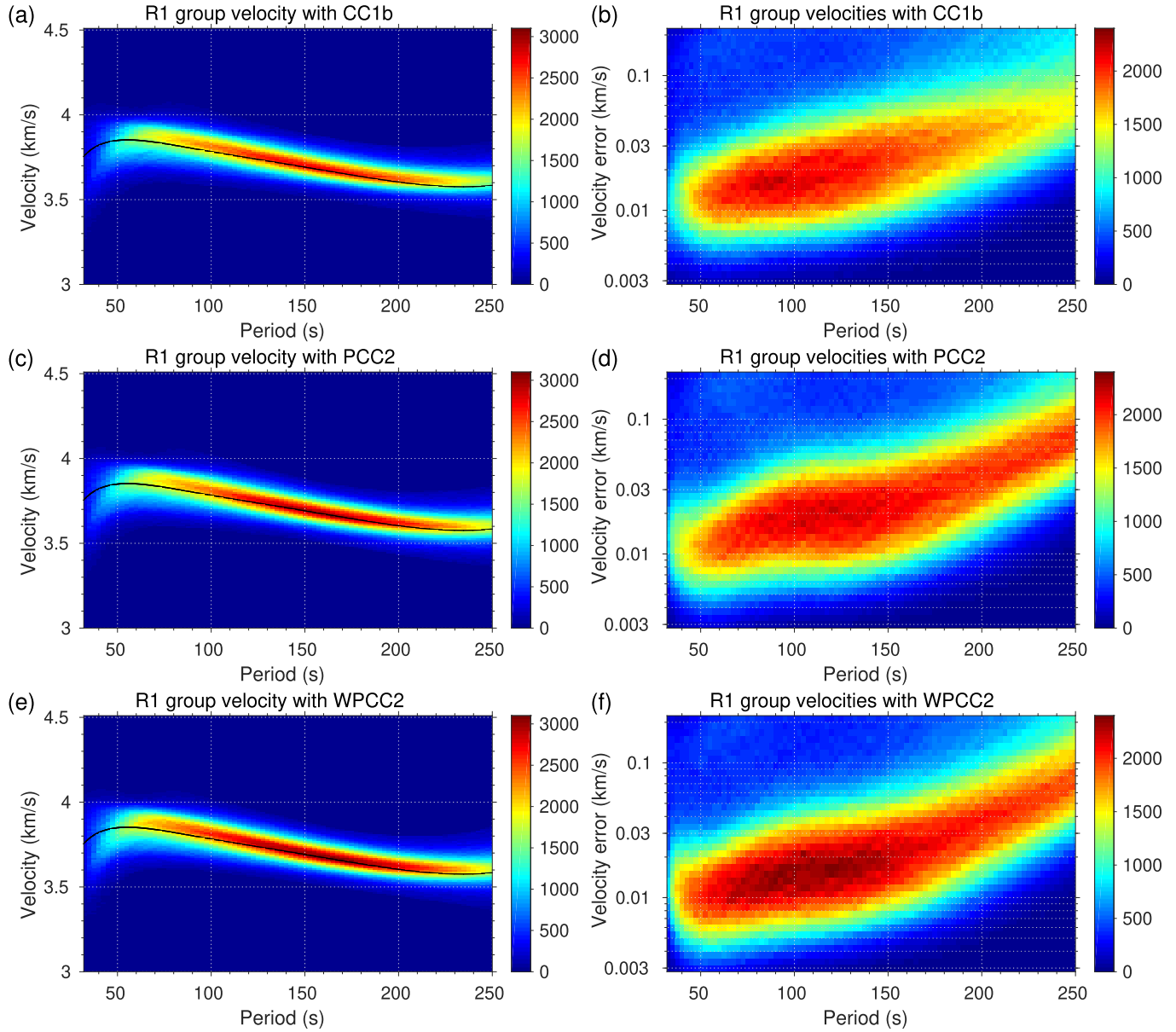


Fig. 8. Histogram of Rayleigh group-velocity observations extracted from (a) spectrally-whitened CC1b, (c) PCC2, and (e) WPCC2 per period and velocity, where the black line is the PREM group velocity, and the standard deviation error of (b) CC1b, (d) PCC2, and (f) WPCC2 observations measured with jackknife resampling.

Network (MN), New Zealand National Seismograph Network (NZ), Portuguese National Seismic Network (PM), Pacific21 Network (PS), United States National Seismic Network (US), Regional Integrated MultiHazard Early Warning System (RM), Seismic Network of Tunisia (TT), and IPY POLENET-Antarctica (YT).

The preprocessing flow consists in correcting the raw data to ground velocity, bandpass filtering from 4 to 32 mHz, decimating to 0.25 samples/s, dividing into one-day-long non-overlapping sequences, and rejecting sequences containing gaps or high-amplitude signals. We compute correlations up to a maximum lag time of  $\pm 12\,000$  s using CC1b, whitening sequences by their average spectra in advance, PCC2 and WPCC2 with a Morlet wavelet with  $\xi_0 = \pi(2/\ln 2)^{1/2}$ , four voices per octave and no decimation. Afterward, we

reject correlations with anomalous energy levels due to, e.g., earthquake coda, and measure the average and the confidence interval of Rayleigh group and phase velocities of the ensemble of daily correlations per station pair through resampling strategies [52]. Jackknife resampling [53] is an objective method to estimate an upper limit of variance, in contrast to conventional methods that arbitrary define uncertainty at, e.g., a percentage of the amplitude of group-velocity maxima in frequency-time analysis (FTAN). Essentially, we apply Jackknife resampling arranging daily correlations in 15 groups (i.e., number of observations) and using two deletions. Then, for each Jackknife sample, we stack the correlations with the two-stage ts-PWS [24] using weights to promote the correlations from quiet days. And finally, we measure group velocity with FTAN, e.g., [12], [54], [55], [56], and phase

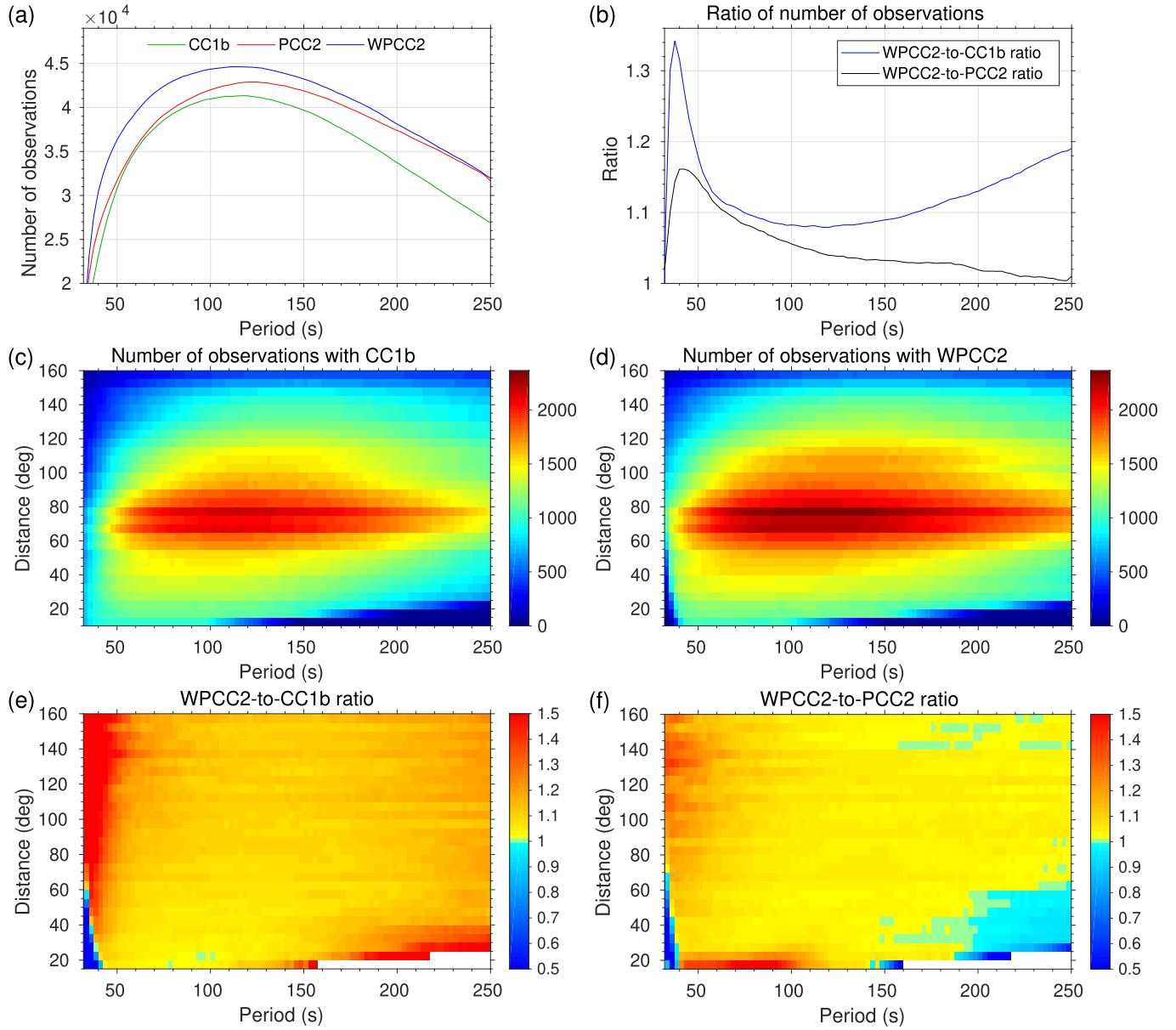


Fig. 9. Comparison of the number of group-velocity observations extracted from ambient noise with the CC1b, PCC2, and WPCC2 methods. (a) Number of observations extracted for CC1b (green), PCC2 (red), and WPCC2 (blue) from the ensemble (56 343) of ambient-noise correlations, and (b) their WPCC2-to-CC1b and WPCC2-to-PCC2 observation ratios per period. Number of velocity observations from (c) CC1b and (d) WPCC2, and their (e) WPCC2-to-CC1b and (f) WPCC2-to-PCC2 observation ratios per period and interstation distance.

velocity using Seislib [57], [58]. FTAN is sufficient for extracting fundamental dispersion curves properly. More advanced methods are useful to, e.g., measure dispersion curves from different modes [59], [60] or automatically distinguish the fundamental mode and the first overtone from noise using deep learning [61].

Fig. 6 shows the EGF and its amplitude spectrum from pairs of stations at several interstation distances, and Fig. 7 displays the Rayleigh group-velocity dispersion curves extracted with the FTAN method. In Fig. 6(a)–(c), we can observe clear signals from minor- and major-arc Rayleigh waves ( $R1$  and  $R2$ ) using CC1b with spectral whitening and PCC2 and WPCC2 without. The SNR of the EGFs extracted with CC1b is lower than with PCC2 and WPCC2. But the

most important difference lies in the frequency spectra of these signals, Fig. 6(d). The amplitude spectra of PCC2 and WPCC2 below 10 mHz, where the signal is stronger, is very similar, while the amplitude of CC1b is generally lower. At higher frequencies, the energy of the correlated signal decreases significantly, mainly due to the increase of attenuation with interstation distance and frequency. In this scenario, the WPCC2 attains a stronger signal and an overall flatter spectrum due to the higher SNR at these frequency bands and the better adaptation of the envelope normalization to the signals in each band. As shown below, the broadband EGFs extracted with WPCC2 enable for robust high-frequency measurements of velocity dispersion. Equally important is removing anomalous correlations and weighting the others in

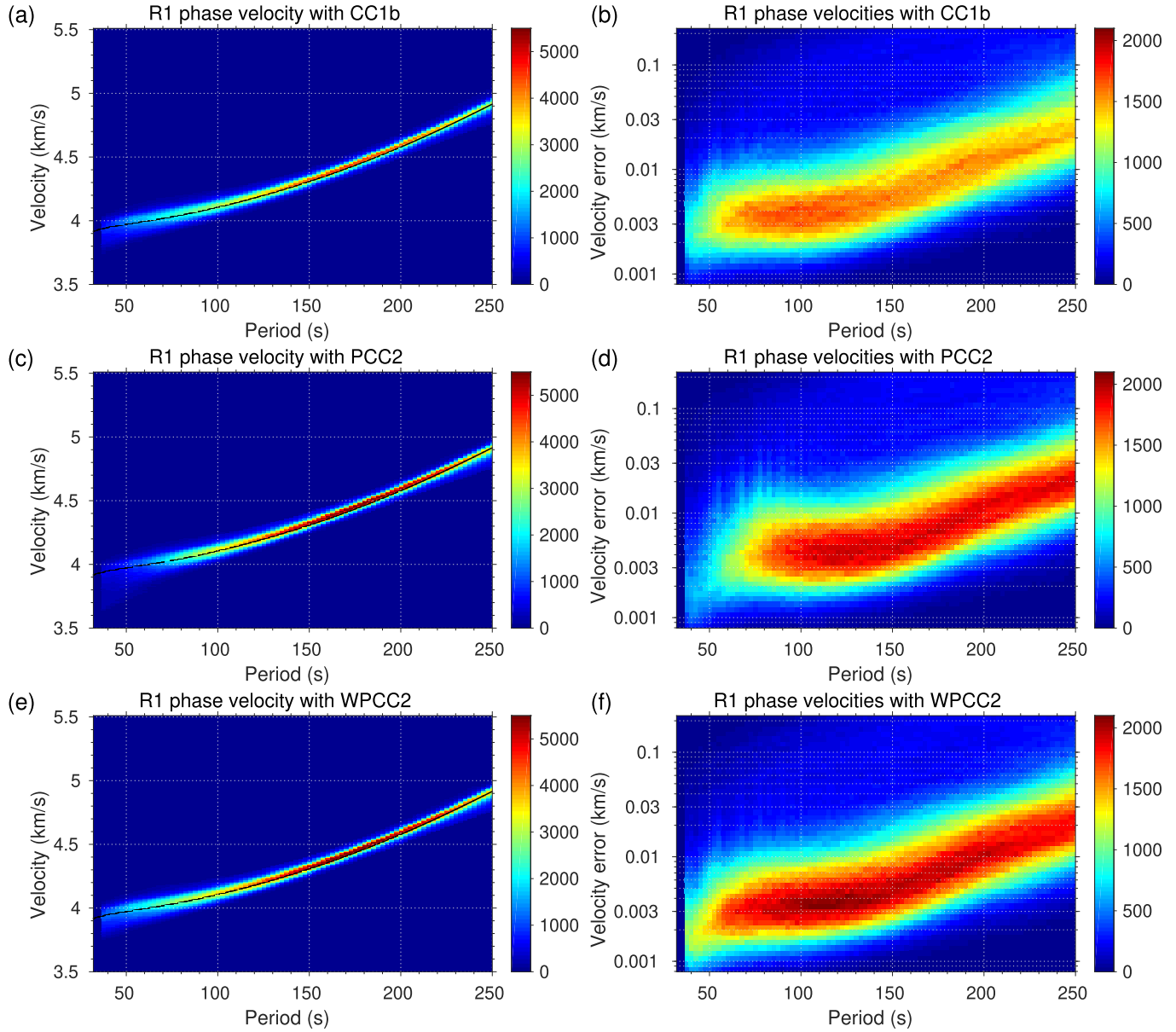


Fig. 10. Histogram of Rayleigh phase-velocity observations extracted from (a) spectrally-whitened CC1b, (c) PCC2, and (e) WPCC2 per period and velocity, where the black line is the PREM group velocity, and the standard deviation error of (b) CC1b, (d) PCC2, and (f) WPCC2 observations measured with jackknife resampling.

the ts-PWS stacking to reject signals from earthquake coda, main source of body-wave energy in this frequency band. Both methods complement each other in obtaining high-quality broadband velocity-dispersion measurements while minimizing interference from body-wave signals. The phase and group velocities extracted from these signals, Fig. 7, with these cross-correlation methods are close at most periods because the large amount of data available assures a good convergence to the EGF. Their confidence intervals decrease with interstation distance, increase with period and, overall, are a bit better for WPCC2. The single exception is for the MPG-HDC station pair, located along the north coast of South America, where CC1b is less robust than PCC2 and WPCC2 probably due to the extreme uneven noise distribution near the coastline. The Rayleigh-wave signal extracted with CC1b is much weaker

and its group velocity is biased toward high velocities at long periods.

The analysis of the accuracy and of potential bias is better done using the ensemble of ambient-noise correlations. The distribution of group-velocity observations of CC1b [see Fig. 8(a)], PCC2 [see Fig. 8(c)], and WPCC2 [see Fig. 8(e)] are similar, in agreement with Fig. 7, and close to the group velocity predicted by the PREM 1-D global model. Nevertheless, when we compare the distributions of their confidence intervals for standard deviation, we observe that WPCC2 [see Fig. 8(f)] leads to more accurate velocities at periods shorter than about 130 s than CC1b [see Fig. 8(b)] and PCC2 [see Fig. 8(d)], and to approximately equally accurate velocities at longer periods. The main difference is on the number of observations (see Fig. 9). The WPCC2 method obtains more

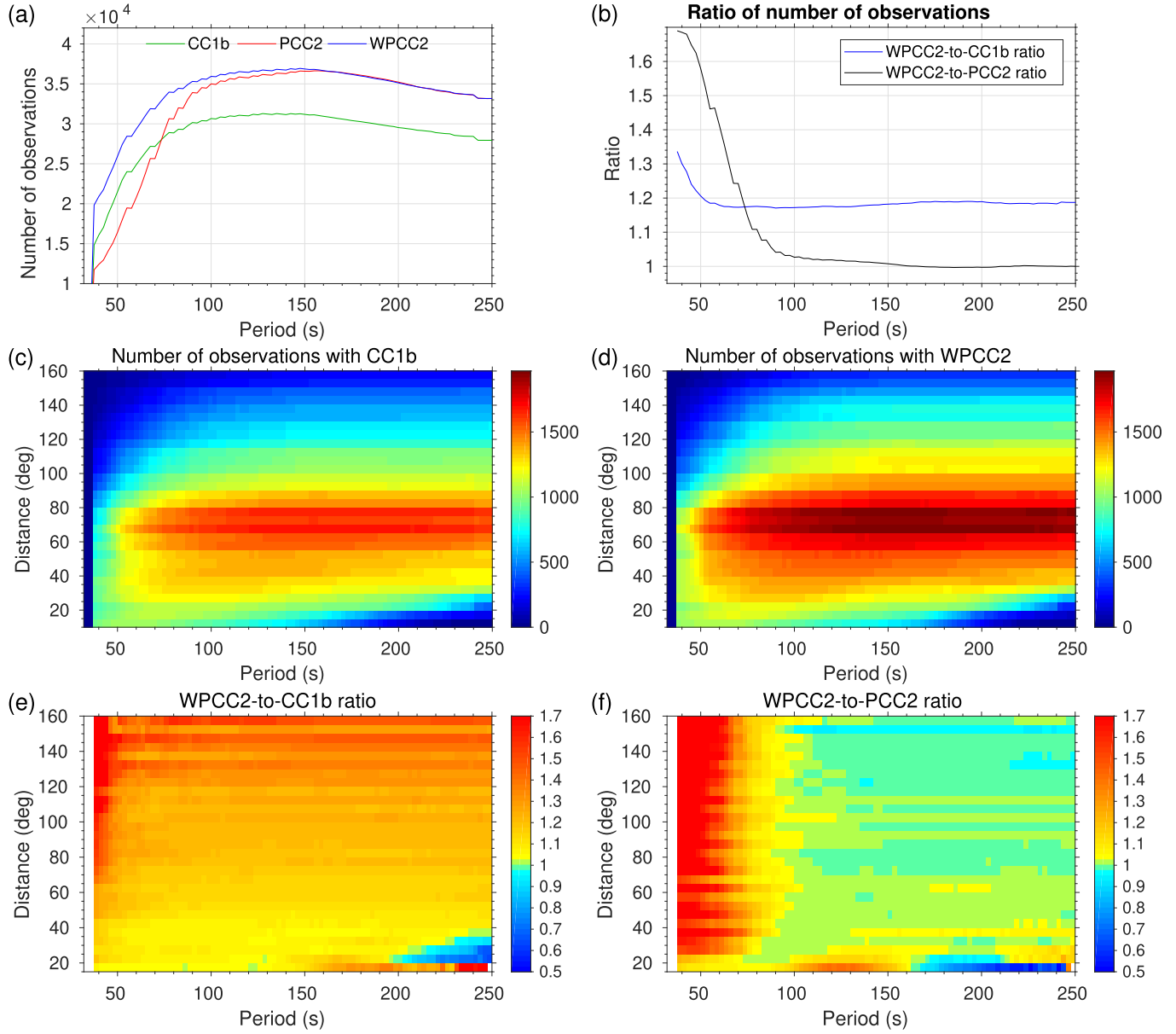


Fig. 11. Comparison of the number of Phase-velocity observations extracted from ambient noise with the CC1b, PCC2, and WPCC2 methods. (a) Number of observations extracted for CC1b (green), PCC2 (red), and WPCC2 (blue) from the ensemble (56 343) of ambient-noise correlations, and (b) their WPCC-to-CC1b and WPCC2-to-PCC2 observation ratios per period. Number of velocity observations from (c) CC1b and (d) WPCC2, and their (e) WPCC2-to-CC1b and (f) WPCC2-to-PCC2 observation ratios per period and interstation distance.

observations than CC1b at all periods and than PCC2 at short periods [see Fig. 9(a) and 9(b)]. More precisely, WPCC2 provides more observations than CC1b at all epicentral distances and periods [see Fig. 9(e)]. This difference increases at long and short periods and reaches the maximum at 40 s, where WPCC2 obtains 34% more observations than CC1b [see Fig. 9(b)]. In contrast, the number of observations obtained with PCC2 and WPCC2 at long periods, where the energy of the correlated signals is higher, are approximately equal or slightly larger for WPCC2. This difference increases as the period reduces until 40 s where WPCC2 obtains 16% more observations than PCC2. At the epicentral distances and periods where we get most of the observations, we do not observe any significant variations with interstation distance

[see Fig. 9(d) and 9(f)]. Far from this area, WPCC2 performs much better at very short distances and a bit worse compared to PCC2 at long periods up to an interstation distance of  $60^\circ$ .

Analyzing the distribution, confidence interval and number of the phase velocity observations, Figs. 10 and 11, yield results equivalent to the group-velocity analysis. WPCC2 obtains more accurate phase velocities at short periods than CC1b and PCC2, and provides more observations than CC1b at all periods and than PCC2 at short periods [see Fig. 11(a) and 11(b)]. Moreover, the ratio of number of observations of WPCC2 to PCC2 increases with interstation distance and at periods shorter than about 50 s, Fig. 11(e), while the WPCC2-to-PCC2 observation ratio remains approximately equal to one at periods longer than 100 s and increases up to 70% at shorter

periods with no clear variation with interstation distance [see Fig. 11(f)].

### C. Computational Cost

WPCC2 offers significant improvements in quality and quantity with a higher computational cost than PCC2. Ventosa et al. [28] show that PCC2 is about two times slower than CC1b, and that its computational cost is mostly determined by seven single-precision FFT operations per cross-correlation. The computational cost of WPCC2 increases linearly with the redundancy of the time-frequency domain decomposition of the frame of wavelets employed and it is mostly determined by three single-precision FFT operations plus four FFT operations per scale. However, WPCC2 allows for an efficient parallelization on the graphics processing unit (GPU) that totally compensates for this increment. In practice, the GPU implementation reduces the wall-clock time cost of WPCC2 to about the cost of PCC2 computed on the central processing unit (CPU) for the relatively high redundancy of the frames used in this article. The exact numbers are strongly machine dependent. In addition, the GPU implementation can accelerate the whole processing flow compared to PCC2 if other tasks, such as data resampling, stacking or dispersion curve extraction, are executed in parallel and profit from the CPU resources released. For instance, in Section III-B, data resampling and subsequent stacking and dispersion curve extraction are about two or three times slower than WPCC2 computed concurrently on the GPU. The current implementation of the WPCC2 method on the GPU is thus fast enough to our needs but has room for improvement regarding the reduction of redundancy and the better exploitation of the computational resources of the most modern GPUs.

## IV. DISCUSSION AND CONCLUSION

We have introduced a frequency-dependent PCC (WPCC) approach to further improve signal extraction from ambient noise or coda correlations. Although ambient-noise or coda correlation studies are being performed at all scales, we focused our work to the extraction of low-frequency signals. Without any loss of generality, our approach is applicable at different scales and for different applications.

The fundamental ingredient of PCC is to measure similarity as phase coherence. Similarly, WPCC measures similarity as phase coherence in the time-scale domain. Both approaches are amplitude unbiased and reduce the influence of poorly distributed high-energy sources, the key difference between them is on the scope of the phase (phasor) measurement. Essentially, the PCC method gets instantaneous unitary phasors by using the Hilbert transform to calculate the dual pair of a time series and form its analytic signal representation [62], and then dividing the resulting signal by its envelope. Considering that the Hilbert transform has a very slow decay ( $1/|t|$ ), the instantaneous phase estimation at a given time sample is affected by samples far from it (strictly the Hilbert function has infinite support). Alternatively, the analytic wavelet functions used in WPCC, such as the Morlet wavelet in the examples above, form a dual pair with a compact time-frequency support and a

much faster decay [43]. Hence, the unitary phasors computed in the WPCC method are affected only by the portion of the time series within the time support of a (pseudo-)analytic wavelet function. This allows us to better adapt the time-frequency resolution of the wavelet function to the correlation length of the signals and the strong amplitude variations in time and frequency of the ambient-noise sources, and extract more information from seismic data.

Wavelet cospectra, e.g., [40] employ the wavelet transform to measure instantaneous scale-wise amplitude and phase differences between two data segments. These instantaneous phase differences are useful to measure small lag times in monitoring studies [41], [42], but often require smoothing to improve robustness and, especially at short periods, may easily lead to cycle skipping problems in case of moderate velocity variations. In contrast, the lag time measures of wavelet cross-correlation based functions comprise the whole data sequences, attain much bigger lag times, and naturally account for the smoothing.

WPCC2 can extract a robust signal or the EGF from seismic ambient-noise data with a broader and more balanced frequency spectrum thanks to its better adaptation to the nonstationary time- and frequency-dependent nature of seismic signals. These skills are important for a better exploitation of seismic data. For instance, in tomography studies, the gains in SNR and frequency distribution usually translate into more paths and more accurate surface-wave velocity-dispersion measurements covering a broader frequency band. Resolving periods where signals are weaker, such as often the short periods, is important to better constraint depth inversions. In full analogy to WPCC2, the normalized wavelet cross-correlation (7) and the WPCC (9) with  $v = 1$  can allow for parallel enhancements compared to NCC and PCC with  $v = 1$ .

No special preprocessing, such as spectral whitening or FTN [13], is required thanks to the automatic data adaptive balancing of the time-frequency spectral contents done through the wavelet transform. WPCC2 is, however, similar in spirit to FTN followed by NCC in the sense that both methods decompose seismic data in time and frequency using a set of filters and then divide the result by the envelope, estimated as the modulus of an analytic signal. The key differences are: 1) WPCC2 is constructed as a single cross-correlation function and 2) FTN whitening uses filters of constant bandwidth (set to one-fourth of the lowest target frequency) and constant time resolution, while WPCC2 uses filters of constant quality (i.e., bandwidth proportional to the central frequency of the filter) and time resolution proportional to the central period. Using constant quality reduces the number of filters significantly in the analysis of broadband signals and, more importantly, the family of wavelets (i.e., the impulse response of the filters) is symmetric and has the same shape at all scales, which is key to be able to adapt to strong amplitude variations of ambient-noise sources equally fast (in number of cycles) at all frequency bands.

In practice, what often does help to improve signal quality is to select or weight the cross-correlations subsequently stacked to promote the signals of interest and suppress the signals of disinterest, e.g., [14], [19], [20]. Shirzad et al. [15] take

selection and weighting one step further by weighting key portions of the cross-correlations, as short as one cycle of the longest target period, according to the inverse of their root-mean-square value and the energy coherence to improve the balance of sources. The correlation of unitary phasors done in PCC and WPCC intrinsically normalize data by its amplitude. This constitutes a less-aggressive alternative to improve the balance of sources and leave further selection and weighting for the stacking stage.

Selection and weighting proved of importance in the hum cross-correlations (see Section III-B) to reduce the contribution of coda waves [63], [64] into the interstation cross-correlations. Rejecting a few cross-correlations with an anomalous energy level and weighting the rest, attenuated by a factor of 10 most of the body-wave signals observed in the EGFs. A more strict selection criteria does not improve significantly body-wave attenuation and worsen the quality and significance of the direct surface-wave EGFs extracted. Even though their full suppression was not possible, whether the remaining body-wave signal is generated by weak coda waves or seismic ambient noise, the quality of the EGFs extracted was good enough to measure surface-wave group-velocity dispersion curves for the big majority of station pairs available with a good quality.

In conclusion, WPCC extracts high-quality broadband EGFs or robust signals computing data-adaptive PCCs between the analytic wavelet decomposition of two seismic data sequences. This approach improves adaptability to the high nonstationary time- and frequency-dependent nature of seismic data compared to conventional, 1-bit and phase cross-correlation methods; and accelerates convergence and increases the number, quality and frequency range of surface-wave velocity observations from seismic hum data, key to resolve short-wavelength and shallow structure in the uppermost mantle. These qualities can easily be extrapolated to different scales/frequencies and help to face current challenges in ambient-noise and coda correlation studies on seismic imaging and monitoring.

## DATA AND RESOURCES

The data used in this study were obtained from the Incorporated Research Institutions of Seismology (IRIS) and the European Integrated Data Archive (EIDA). The CPU and GPU accelerated versions of code implementing CC1b, PCC, and WPCC, and the two-stage ts-PWS are open source under the LGPL v3 license and available at <https://github.com/sergiventosa/FastPCC>, and at <https://github.com/sergiventosa/ts-PWS>.

## APPENDIX A

The proof of (3) is similar to the proof of the wavelet reconstruction formula, e.g., [43], [44]. The Fourier transform of the data vectors  $x$  and  $y$  decomposed in the time-scale domain with (1) are

$$\hat{x}(\omega, \lambda) = \hat{x}(\omega)\sqrt{\lambda}\hat{\psi}^*(\lambda\omega) \quad (12)$$

$$\hat{y}(\omega, \lambda) = \hat{y}(\omega)\sqrt{\lambda}\hat{\psi}^*(\lambda\omega) \quad (13)$$

considering  $\mathcal{F}\{\psi^*(-t)\} = \psi^*(\omega)$ , and the wavelet cross-correlation of them, (2), is given by

$$\hat{c}_{xy}(\omega, \lambda) = \left( \hat{x}(\omega)\sqrt{\lambda}\hat{\psi}^*(\lambda\omega) \right)^* \left( \hat{y}(\omega)\sqrt{\lambda}\hat{\psi}^*(\lambda\omega) \right) \quad (14)$$

$$= \hat{x}^*(\omega)\sqrt{\lambda}\hat{\psi}^*(\lambda\omega)\hat{y}(\omega)\sqrt{\lambda}\hat{\psi}^*(\lambda\omega). \quad (15)$$

Then, introducing  $\hat{c}_{xy}(\omega, \lambda)$  in the Fourier transform of  $c_{xy}(\tau)$ , (3)

$$\hat{c}_{xy}(\omega) = \frac{1}{C_\psi} \int_0^\infty \hat{c}_{xy}(\omega, \lambda) \frac{d\lambda}{\lambda^2} \quad (16)$$

$$= \hat{x}^*(\omega)\hat{y}(\omega) \frac{1}{C_\psi} \int_0^\infty \frac{|\hat{\psi}(\lambda\omega)|^2}{\lambda} d\lambda \quad (17)$$

and applying the change of variables  $\xi = \lambda\omega$  prove that

$$\hat{c}_{xy}(\omega) = \hat{x}^*(\omega)\hat{y}(\omega) \frac{1}{C_\psi} \int_0^\infty \frac{|\hat{\psi}(\xi)|^2}{\xi} d\xi \quad (18)$$

and thus the admissibility condition

$$C_\psi = \int_0^\infty \frac{|\hat{\psi}(\xi)|^2}{\xi} d\xi \quad (19)$$

used in the recomposition of the standard cross-correlation function from the wavelet cross-correlation.

## APPENDIX B

Frames of wavelets are a common choice to sample the time-frequency domain according to the actual resolution of the CWT. Very briefly, the sampling along the scale axis is logarithmic,  $\lambda = a^s$ , and along the time axis proportional to period,  $\tau = ua^s b$ , where  $s$  is the scale index,  $u$  is the lag-time index,  $a > 1$  is fixed, and  $b > 0$  is the sampling period at the scale  $s = 0$  ( $\lambda = 1$ ). Then, the wavelet coefficient  $x[u, s]$  of the input data  $x$  is

$$x[u, s] = \int_{-\infty}^\infty x(t)\psi_{u,s}^*(t)dt \quad (20)$$

with

$$\psi_{u,s}(t) = \frac{1}{a^{s/2}}\psi\left(\frac{t - ua^s b}{a^s}\right). \quad (21)$$

We can reconstruct  $x$  from its wavelet coefficients by defining a frame of  $L^2(\mathbb{R})$ ,  $\phi_m(t) = a^{-s/2}\psi_{u,s}(t)$ , with frame bounds  $0 < A \leq B < \infty$  that satisfies

$$A \leq \frac{1}{b} \sum_s |\hat{\psi}(a^s \omega)|^2 \leq B \quad \forall \omega \in \mathbb{R} - \{0\}. \quad (22)$$

Then, the pseudo-inverse of this frame, the dual frame  $\tilde{\phi}_m(t) = a^{-s/2}\tilde{\psi}_{u,s}(t)$ , is well defined and the input data  $x$  can be recomposed by

$$x(t) = \sum_{u,s} \frac{1}{a^s} x[u, s] \tilde{\psi}_{u,s}(t). \quad (23)$$

For increasing redundancies, this frame tends to a tight frame and its dual frame can be well approximated as

$$\tilde{\psi}(t) = \frac{2}{A + B} \psi(t) \quad \text{with} \quad A \simeq \frac{C_\psi}{b \ln a} \simeq B. \quad (24)$$

Finally, we need to discretize the frame of continuous wavelet functions to compute the wavelet transform of the

input sequences. This is conventionally done by setting  $t = nT$  and  $a = 2^{1/V}$  in (21) where  $n$  is the sample index,  $T$  is the sampling period, and  $V \in \mathbb{N}$  is the number of voices. Therefore, under the tight frame approximation, the frame coefficients are given by

$$x[u, s] = \sum_n x[n] \psi_{u,s}^*[n] \quad (25)$$

with

$$\psi_{u,s}[n] = \frac{1}{2^{s/2V}} \psi\left(\frac{nT - u2^{\lfloor s/V \rfloor}b}{2^{s/V}}\right) \quad (26)$$

and the input data sequence is reconstructed by

$$x[n] \simeq \frac{b\ln 2}{VC_\psi} \sum_{u,s} \frac{1}{2^{s/V}} x[u, s] \psi_{u,s}[n] \quad (27)$$

where  $\lfloor s/V \rfloor$  is the lower integer part of  $s/V$ .

#### ACKNOWLEDGMENT

Numerical computations were partly performed on the Earth cluster of the Geosciences Barcelona, CSIC, Barcelona, Spain. The authors would like to thank associate editor M. D. Sacchi and two anonymous reviewers for constructive reviews.

#### REFERENCES

- [1] Y. Yang, M. H. Ritzwoller, A. L. Levshin, and N. M. Shapiro, "Ambient noise Rayleigh wave tomography across Europe," *Geophys. J. Int.*, vol. 168, no. 1, pp. 259–274, Jan. 2007, doi: [10.1111/j.1365-246X.2006.03203.x](https://doi.org/10.1111/j.1365-246X.2006.03203.x).
- [2] E. Saygin and B. L. N. Kennett, "Crustal structure of Australia from ambient seismic noise tomography," *J. Geophys. Res., Solid Earth*, vol. 117, no. B1, Jan. 2012, Art. no. B01304, doi: [10.1029/2011JB008403](https://doi.org/10.1029/2011JB008403).
- [3] W. Shen and M. H. Ritzwoller, "Crustal and uppermost mantle structure beneath the United States," *J. Geophys. Res., Solid Earth*, vol. 121, no. 6, pp. 4306–4342, Jun. 2016, doi: [10.1002/2016JB012887](https://doi.org/10.1002/2016JB012887).
- [4] Y. Lu, L. Stehly, and A. Paul, "High-resolution surface wave tomography of the European crust and uppermost mantle from ambient seismic noise," *Geophys. J. Int.*, vol. 214, no. 2, pp. 1136–1150, Aug. 2018, doi: [10.1093/gji/ggy188](https://doi.org/10.1093/gji/ggy188).
- [5] J. Ritsema and V. Lekić, "Heterogeneity of seismic wave velocity in Earth's mantle," *Annu. Rev. Earth Planet. Sci.*, vol. 48, no. 1, pp. 377–401, May 2020, doi: [10.1146/annurev-earth-082119-065909](https://doi.org/10.1146/annurev-earth-082119-065909).
- [6] K. Nishida, J.-P. Montagner, and H. Kawakatsu, "Global surface wave tomography using seismic hum," *Science*, vol. 326, no. 5949, p. 112, Oct. 2009, doi: [10.1126/science.1176389](https://doi.org/10.1126/science.1176389).
- [7] A. Haned, E. Stutzmann, M. Schimmel, S. Kiseley, A. Davaille, and A. Yelles-Chaouche, "Global tomography using seismic hum," *Geophys. J. Int.*, vol. 204, no. 2, pp. 1222–1236, Dec. 2015, doi: [10.1093/gji/ggv516](https://doi.org/10.1093/gji/ggv516).
- [8] F. Ardhuin, L. Gualtieri, and E. Stutzmann, "How ocean waves rock the Earth: Two mechanisms explain microseisms with periods 3 to 300 s," *Geophys. Res. Lett.*, vol. 42, no. 3, pp. 765–772, Feb. 2015, doi: [10.1002/2014GL062782](https://doi.org/10.1002/2014GL062782).
- [9] N. M. Shapiro and M. Campillo, "Emergence of broadband Rayleigh waves from correlations of the ambient seismic noise," *Geophys. Res. Lett.*, vol. 31, no. 7, pp. 1–4, 2004, I07614, doi: [10.1029/2004GL019491](https://doi.org/10.1029/2004GL019491).
- [10] K. Wapenaar, E. Slob, R. Snieder, and A. Curtis, "Tutorial on seismic interferometry: Part 2—Underlying theory and new advances," *Geophysics*, vol. 75, no. 5, pp. 75A211–75A227, Sep. 2010, doi: [10.1190/1.3463440](https://doi.org/10.1190/1.3463440).
- [11] M. Campillo and P. Roux, "Crust and lithospheric structure—Seismic imaging and monitoring with ambient noise correlations," in *Treatise on Geophysics*, 2nd ed., G. Schubert, Ed. Oxford, U.K.: Elsevier, 2015, ch. 1.12, pp. 391–417, doi: [10.1016/B978-0-444-53802-4.00024-5](https://doi.org/10.1016/B978-0-444-53802-4.00024-5).
- [12] G. D. Bensen et al., "Processing seismic ambient noise data to obtain reliable broad-band surface wave dispersion measurements," *Geophys. J. Int.*, vol. 169, no. 3, pp. 1239–1260, Jun. 2007, doi: [10.1111/j.1365-246x.2007.03374.x](https://doi.org/10.1111/j.1365-246x.2007.03374.x).
- [13] Y. Shen, Y. Ren, H. Gao, and B. Savage, "An improved method to extract very-broadband empirical Green's functions from ambient seismic noise," *Bull. Seismol. Soc. Amer.*, vol. 102, no. 4, pp. 1872–1877, Aug. 2012, doi: [10.1785/0120120023](https://doi.org/10.1785/0120120023).
- [14] M. H. Ritzwoller and L. Feng, "Overview of pre- and post-processing of ambient-noise correlations," in *Seismic Ambient Noise*. Cambridge, U.K.: Cambridge Univ. Press, 2019, ch. 5, pp. 144–187, doi: [10.1017/9781108264808.007](https://doi.org/10.1017/9781108264808.007).
- [15] T. Shirzad, M. Safarkhani, and M. S. Assumpção, "Extracting reliable empirical Green's functions using weighted cross-correlation functions of ambient seismic noise in west-central and Southern Brazil," *Geophys. J. Int.*, vol. 230, no. 2, pp. 1441–1464, May 2022, doi: [10.1093/gji/gjac126](https://doi.org/10.1093/gji/gjac126).
- [16] P. Cupillard, L. Stehly, and B. Romanowicz, "The one-bit noise correlation: A theory based on the concepts of coherent and incoherent noise," *Geophys. J. Int.*, vol. 184, no. 3, pp. 1397–1414, Mar. 2011, doi: [10.1111/j.1365-246x.2010.04923.x](https://doi.org/10.1111/j.1365-246x.2010.04923.x).
- [17] H. A. Pedersen and F. Krüger, "Influence of the seismic noise characteristics on noise correlations in the Baltic shield," *Geophys. J. Int.*, vol. 168, no. 1, pp. 197–210, Jan. 2007, doi: [10.1111/j.1365-246x.2006.03177.x](https://doi.org/10.1111/j.1365-246x.2006.03177.x).
- [18] M. Schimmel et al., "Seismic noise autocorrelations on Mars," *Earth Space Sci.*, vol. 8, no. 6, Jun. 2021, Art. no. e2021EA001755, doi: [10.1029/2021EA001755](https://doi.org/10.1029/2021EA001755).
- [19] P. Boué, P. Poli, M. Campillo, and P. Roux, "Reverberations, coda waves and ambient noise: Correlations at the global scale and retrieval of the deep phases," *Earth Planet. Sci. Lett.*, vol. 391, pp. 137–145, Apr. 2014, doi: [10.1016/j.epsl.2014.01.047](https://doi.org/10.1016/j.epsl.2014.01.047).
- [20] J. Xie, Y. Yang, and Y. Luo, "Improving cross-correlations of ambient noise using an RMS-ratio selection stacking method," *Geophys. J. Int.*, vol. 222, no. 1, pp. 989–1002, Mar. 2020, doi: [10.1093/gji/ggaa232](https://doi.org/10.1093/gji/ggaa232).
- [21] M. Schimmel and J. Gallart, "Frequency-dependent phase coherence for noise suppression in seismic array data," *J. Geophys. Res., Solid Earth*, vol. 112, no. B4, Apr. 2007, Art. no. b04303, doi: [10.1029/2006JB004680](https://doi.org/10.1029/2006JB004680).
- [22] A. M. Baig, M. Campillo, and F. Brenguier, "Denoising seismic noise cross correlations," *J. Geophys. Res.*, vol. 114, no. B8, 2009, Art. no. b08310, doi: [10.1029/2008JB006085](https://doi.org/10.1029/2008JB006085).
- [23] M. Schimmel, E. Stutzmann, and J. Gallart, "Using instantaneous phase coherence for signal extraction from ambient noise data at a local to a global scale," *Geophys. J. Int.*, vol. 184, no. 1, pp. 494–506, Jan. 2011, doi: [10.1111/j.1365-246x.2010.04861.x](https://doi.org/10.1111/j.1365-246x.2010.04861.x).
- [24] S. Ventosa, M. Schimmel, and E. Stutzmann, "Extracting surface waves, hum and normal modes: Time-scale phase-weighted stack and beyond," *Geophys. J. Int.*, vol. 211, no. 1, pp. 30–44, Oct. 2017, doi: [10.1093/gji/ggx284](https://doi.org/10.1093/gji/ggx284).
- [25] L. Moreau, L. Stehly, P. Boué, Y. Lu, E. Larose, and M. Campillo, "Improving ambient noise correlation functions with an SVD-based Wiener filter," *Geophys. J. Int.*, vol. 211, no. 1, pp. 418–426, Oct. 2017, doi: [10.1093/gji/ggx306](https://doi.org/10.1093/gji/ggx306).
- [26] M. Schimmel, E. Stutzmann, and S. Ventosa, "Low-frequency ambient noise autocorrelations: Waveforms and normal modes," *Seismol. Res. Lett.*, vol. 89, no. 4, pp. 1488–1496, Jul. 2018, doi: [10.1785/0220180027](https://doi.org/10.1785/0220180027).
- [27] M. Schimmel, "Phase cross-correlations: Design, comparisons, and applications," *Bull. Seismol. Soc. Amer.*, vol. 89, no. 5, pp. 1366–1378, Oct. 1999, doi: [10.1785/BSSA0890051366](https://doi.org/10.1785/BSSA0890051366).
- [28] S. Ventosa, M. Schimmel, and E. Stutzmann, "Towards the processing of large data volumes with phase cross-correlation," *Seismol. Res. Lett.*, vol. 90, no. 4, pp. 1663–1669, May 2019, doi: [10.1785/0220190022](https://doi.org/10.1785/0220190022).
- [29] V. D'Hour, M. Schimmel, A. F. Do Nascimento, J. M. Ferreira, and H. C. Lima Neto, "Detection of subtle hydromechanical medium changes caused by a small-magnitude earthquake swarm in NE Brazil," *Pure Appl. Geophys.*, vol. 173, no. 4, pp. 1097–1113, Apr. 2016, doi: [10.1007/s00024-015-1156-0](https://doi.org/10.1007/s00024-015-1156-0).
- [30] P. Sánchez-Pastor, A. Obermann, and M. Schimmel, "Detecting and locating precursory signals during the 2011 El Hierro, Canary Islands, submarine eruption," *Geophys. Res. Lett.*, vol. 45, no. 19, p. 10, Oct. 2018, doi: [10.1029/2018GL079550](https://doi.org/10.1029/2018GL079550).
- [31] P. Sánchez-Pastor et al., "Imaging high-temperature geothermal reservoirs with ambient seismic noise tomography, a case study of the Hengill geothermal field, SW Iceland," *Geothermics*, vol. 96, Nov. 2021, Art. no. 102207, doi: [10.1016/j.geothermics.2021.102207](https://doi.org/10.1016/j.geothermics.2021.102207).
- [32] G. Taylor, S. Rost, and G. Houseman, "Crustal imaging across the North Anatolian Fault zone from the autocorrelation of ambient seismic noise," *Geophys. Res. Lett.*, vol. 43, no. 6, pp. 2502–2509, Mar. 2016, doi: [10.1002/2016GL067715](https://doi.org/10.1002/2016GL067715).

- [33] G. Becker and B. Knapmeyer-Endrun, "Crustal thickness across the trans-European suture zone from ambient noise autocorrelations," *Geophys. J. Int.*, vol. 212, no. 2, pp. 1237–1254, Feb. 2018, doi: [10.1093/gji/ggx485](https://doi.org/10.1093/gji/ggx485).
- [34] T. N. Ashruf and A. Morelli, "The moho reflectivity of the subduction beneath the southwestern Alps from ambient seismic noise autocorrelations," *Geophys. J. Int.*, vol. 230, no. 1, pp. 298–316, Mar. 2022, doi: [10.1093/gji/ggac079](https://doi.org/10.1093/gji/ggac079).
- [35] P. Romero and M. Schimmel, "Mapping the basement of the Ebro Basin in Spain with seismic ambient noise autocorrelations," *J. Geophys. Res., Solid Earth*, vol. 123, no. 6, pp. 5052–5067, Jun. 2018, doi: [10.1029/2018JB015498](https://doi.org/10.1029/2018JB015498).
- [36] X. Ma and H. Tkalcic, "CCREM: New reference Earth model from the global coda-correlation wavefield," *J. Geophys. Res., Solid Earth*, vol. 126, no. 9, Sep. 2021, Art. no. e2021JB022515, doi: [10.1029/2021JB022515](https://doi.org/10.1029/2021JB022515).
- [37] J. Acevedo, G. Fernández-Viejo, S. Llana-Fúnez, C. López-Fernández, J. Olona, and D. Pérez-Millán, "Radial anisotropy and S-wave velocity depict the internal to external zone transition within the Variscan orogen (NW Iberia)," *Solid Earth*, vol. 13, no. 3, pp. 659–679, Mar. 2022, doi: [10.5194/se-13-659-2022](https://doi.org/10.5194/se-13-659-2022).
- [38] G. Silveira, N. A. Dias, S. Kiselev, E. Stutzmann, S. Custódio, and M. Schimmel, "Imaging the crust and uppermost mantle structure of Portugal (West Iberia) with seismic ambient noise," *Geophys. J. Int.*, vol. 230, no. 2, pp. 1106–1120, Apr. 2022, doi: [10.1093/gji/ggac106](https://doi.org/10.1093/gji/ggac106).
- [39] H. Li and T. Nozaki, "Application of wavelet cross-correlation analysis to a plane turbulent jet," *JSME Int. J. B*, vol. 40, no. 1, pp. 58–66, 1997, doi: [10.1299/jsmib.40.58](https://doi.org/10.1299/jsmib.40.58).
- [40] A. Grinsted, J. C. Moore, and S. Jevrejeva, "Application of the cross wavelet transform and wavelet coherence to geophysical time series," *Nonlinear Processes Geophys.*, vol. 11, nos. 5–6, pp. 561–566, Nov. 2004, doi: [10.5194/npg-11-561-2004](https://doi.org/10.5194/npg-11-561-2004).
- [41] S. Mao, A. Mordret, M. Campillo, H. Fang, and R. D. van der Hilst, "On the measurement of seismic traveltimes changes in the time-frequency domain with wavelet cross-spectrum analysis," *Geophys. J. Int.*, vol. 221, no. 1, pp. 550–568, Dec. 2019, doi: [10.1093/gji/ggz495](https://doi.org/10.1093/gji/ggz495).
- [42] A. Mordret et al., "Noise-based ballistic wave passive seismic monitoring—Part 2: Surface waves," *Geophys. J. Int.*, vol. 221, no. 1, pp. 692–705, Apr. 2020, doi: [10.1093/gji/ggaa016](https://doi.org/10.1093/gji/ggaa016).
- [43] I. Daubechies, *Ten Lectures on Wavelets* (SIAM Lecture Series). Philadelphia, PA, USA: CBMS-NSF, 1992.
- [44] S. Mallat, *A Wavelet Tour of Signal Processing: The Sparse Way*. New York, NY, USA: Academic, 2008.
- [45] S. Ventosa, C. Simon, M. Schimmel, J. J. Danobeitia, and A. Manuel, "The S-transform from a wavelet point of view," *IEEE Trans. Signal Process.*, vol. 56, no. 7, pp. 2771–2780, Jul. 2008, doi: [10.1109/TSP.2008.917029](https://doi.org/10.1109/TSP.2008.917029).
- [46] K. Nishida, "Earth's background free oscillations," *Annu. Rev. Earth Planet. Sci.*, vol. 41, no. 1, pp. 719–740, May 2013, doi: [10.1146/annurev-earth-050212-124020](https://doi.org/10.1146/annurev-earth-050212-124020).
- [47] J. R. Peterson, "Observations and modeling of seismic background noise," U.S. Geol. Surv., Reston, VA, USA, Tech. Rep. 93-322, 1993. [Online]. Available: <http://pubs.er.usgs.gov/publication/ofr93322>
- [48] J. M. Lilly and S. C. Olhede, "Generalized Morse wavelets as a superfamily of analytic wavelets," *IEEE Trans. Signal Process.*, vol. 60, no. 11, pp. 6036–6041, Nov. 2012, doi: [10.1109/TSP.2012.2210890](https://doi.org/10.1109/TSP.2012.2210890).
- [49] E. Stutzmann, "GEOSCOPE station noise levels," *Bull. Seismol. Soc. Amer.*, vol. 90, no. 3, pp. 690–701, Jun. 2000, doi: [10.1785/0119990025](https://doi.org/10.1785/0119990025).
- [50] E. Nuñez, M. Schimmel, D. Stich, and A. Iglesias, "Crustal velocity anomalies in Costa Rica from ambient noise tomography," *Pure Appl. Geophys.*, vol. 177, no. 2, pp. 941–960, Feb. 2020, doi: [10.1007/s00024-019-02315-z](https://doi.org/10.1007/s00024-019-02315-z).
- [51] K. Sager, C. Boehm, L. Ermert, L. Krischer, and A. Fichtner, "Global-scale full-waveform ambient noise inversion," *J. Geophys. Res., Solid Earth*, vol. 125, no. 4, Apr. 2020, Art. no. e2019JB018644, doi: [10.1029/2019JB018644](https://doi.org/10.1029/2019JB018644).
- [52] M. Schimmel, E. Stutzmann, and S. Ventosa, "Measuring group velocity in seismic noise correlation studies based on phase coherence and resampling strategies," *IEEE Trans. Geosci. Remote Sens.*, vol. 55, no. 4, pp. 1928–1935, Apr. 2017, doi: [10.1109/TGRS.2016.2631445](https://doi.org/10.1109/TGRS.2016.2631445).
- [53] B. Efron and C. Stein, "The jackknife estimate of variance," *Ann. Statist.*, vol. 9, no. 3, pp. 586–596, May 1981. [Online]. Available: <http://www.jstor.org/stable/2240822>
- [54] A. Dziewonski, S. Bloch, and M. Landisman, "A technique for the analysis of transient seismic signals," *Bull. Seismol. Soc. Amer.*, vol. 59, no. 1, pp. 427–444, Feb. 1969, doi: [10.1785/BSSA0590010427](https://doi.org/10.1785/BSSA0590010427).
- [55] A. L. Levshin, V. F. Pisarenko, and G. A. Pogrebinsky, "On a frequency-time analysis of oscillations," *Ann. Geophys.*, vol. 28, no. 2, pp. 211–218, 1972. [Online]. Available: <https://oceanrep.geomar.de/id/eprint/46865/>
- [56] A. L. Levshin and M. H. Ritzwoller, "Automated detection, extraction, and measurement of regional surface waves," *Pure Appl. Geophys.*, vol. 158, no. 8, pp. 1531–1545, Aug. 2001, doi: [10.1007/PL00001233](https://doi.org/10.1007/PL00001233).
- [57] F. Magrin, S. Lauro, E. Kästle, and L. Boschi, "Surface-wave tomography using SeisLib: A Python package for multiscale seismic imaging," *Geophys. J. Int.*, vol. 231, no. 2, pp. 1011–1030, Jul. 2022, doi: [10.1093/gji/ggac236](https://doi.org/10.1093/gji/ggac236).
- [58] E. D. Kästle, R. Soomro, C. Weemstra, L. Boschi, and T. Meier, "Two-receiver measurements of phase velocity: Cross-validation of ambient-noise and earthquake-based observations," *Geophys. J. Int.*, vol. 207, no. 3, pp. 1493–1512, Jul. 2016, doi: [10.1093/gji/ggw341](https://doi.org/10.1093/gji/ggw341).
- [59] M. Holschneider, M. S. Diallo, M. Kulesh, M. Ohrnberger, E. Lück, and F. Scherbaum, "Characterization of dispersive surface waves using continuous wavelet transforms," *Geophys. J. Int.*, vol. 163, no. 2, pp. 463–478, Nov. 2005, doi: [10.1111/j.1365-246X.2005.02787.x](https://doi.org/10.1111/j.1365-246X.2005.02787.x).
- [60] R. Takagi and K. Nishida, "Multimode dispersion measurement of surface waves extracted by multicomponent ambient noise cross-correlation functions," *Geophys. J. Int.*, vol. 231, no. 2, pp. 1196–1220, Jul. 2022, doi: [10.1093/gji/ggac225](https://doi.org/10.1093/gji/ggac225).
- [61] X. Zhang, Z. Jia, Z. E. Ross, and R. W. Clayton, "Extracting dispersion curves from ambient noise correlations using deep learning," *IEEE Trans. Geosci. Remote Sens.*, vol. 58, no. 12, pp. 8932–8939, Dec. 2020, doi: [10.1109/TGRS.2020.2992043](https://doi.org/10.1109/TGRS.2020.2992043).
- [62] M. T. Taner, F. Koehler, and R. E. Sheriff, "Complex seismic trace analysis," *Geophysics*, vol. 44, no. 6, pp. 1041–1063, Jun. 1979, doi: [10.1190/1.1440994](https://doi.org/10.1190/1.1440994).
- [63] T. Pham, H. Tkalcic, M. Sambridge, and B. L. N. Kennett, "Earth's correlation wavefield: Late coda correlation," *Geophys. Res. Lett.*, vol. 45, no. 7, pp. 3035–3042, Apr. 2018, doi: [10.1002/2018GL077244](https://doi.org/10.1002/2018GL077244).
- [64] H. Tkalcic, T.-S. Pham, and S. Wang, "The Earth's coda correlation wavefield: Rise of the new paradigm and recent advances," *Earth-Science Rev.*, vol. 208, Sep. 2020, Art. no. 103285, doi: [10.1016/j.earscirev.2020.103285](https://doi.org/10.1016/j.earscirev.2020.103285).



**Sergi Ventosa** received the Engineering degrees in electronics and telecommunication engineering and the Ph.D. degree in the area of data adapting filtering and wavelet design for broadband seismic signal extraction from the Polytechnic University of Catalonia (UPC), Barcelona, Spain, in 1999, 2002, and 2010, respectively.

He was a Post-Doctoral Researcher with IFP Energies Nouvelles, Rueil-Malmaison, France, from 2010 to 2011; the Institut de Physique du Globe de Paris, Paris, France, from 2011 to 2015; and the Geosciences Barcelona (GEO3BCN), CSIC, Barcelona, from 2015 to 2018. He was a Scientific Researcher with the Institute of Marine Sciences (ICM), CSIC, from 2019 to 2020, and GEO3BCN, CSIC, from 2021 to 2022. He currently works with ICM, Department of Marine Geosciences, Barcelona. His research interests include seismic signal detection, ambient noise tomography, deep and shallow Earth's structure, signal processing, inversion theory, and distributed acoustic sensing.



**Martin Schimmel** received the master's degree in geophysics from the University Fridericiana of Karlsruhe, Karlsruhe, Germany, in 1992, and the Ph.D. degree from Utrecht University, Utrecht, The Netherlands, in 1997.

Before becoming a Research Staff Member with the Geosciences Barcelona (GEO3BCN), CSIC, Barcelona, Spain, in 2008, he was a Research Fellow with the Institute of Astronomy and Geophysics, University of São Paulo, São Paulo, Brazil, and GEO3BCN, CSIC. He is a seismologist and his main research interests include the physical phenomena of seismic wave propagation, the detection and understanding of the multitude of seismic signals in seismograms, and the different strategies to image and constrain the structure of the Earth interior. He is experienced and internationally recognized on the detection/identification of weak seismic signals and their use to constrain Earth structure, the study and usage of seismic noise for imaging and monitoring, and the design of independent strategies to enhance seismic signals and/or to turn ambient noise into signals.